MAGNETIC MEMORY IN EXCHANGE BIAS THIN FILMS

by

Brian M Wilcken

A senior thesis submitted to the faculty of

Brigham Young University

in partial fulfillment of the requirements for the degree of

Bachelor of Science

Department of Physics and Astronomy

Brigham Young University

August 2009

BRIGHAM YOUNG UNIVERSITY

DEPARTMENT APPROVAL

of a senior thesis submitted by

Brian M Wilcken

This thesis has been reviewed by the research advisor, research coordinator, and department chair and has been found to be satisfactory.

Date	Karine Chesnel, Advisor
Date	Eric Hintz, Research Coordinator
Date	Ross L. Spencer, Chair

ABSTRACT

MAGNETIC MEMORY IN EXCHANGE BIAS THIN FILMS

Brian M Wilcken

Department of Physics and Astronomy

Bachelor of Science

We have used the technique of coherent X-ray Resonant Magnetic Scattering (XRMS) to probe the magnetic domain morphologies in a $([Co/Pd]_{12}IrMn)_4$ exchange bias thin film. When illuminated by coherent light, the thin film produces specific speckle patterns that reveal information about the local magnetic domain topology in the sample. After subjecting the sample to a variable magnetic field and collecting XRMS patterns, we have analyzed the amount of magnetic memory within the sample by employing a cross-correlation approach. Results indicate that, at low temperature, the sample shows very high magnetic memory in the coercive region of the magnetization cycle. In particular, the system exhibits strong return point memory (RPM) and conjugate point memory (CPM). The dependency of RPM and CPM on applied field will be presented first in a 1D and then in a 2D field analysis showing that the magnetic memory stays stable within the coercive region of the magnetization.

ACKNOWLEDGMENTS

I would like to thank my wife Elizabeth for enduring with me through long hours of writing and editing this thesis. Also, I would like to thank the BYU Department of Physics and Astronomy for providing necessary financial support, so that I could conduct the research necessary in order to finish this thesis. Finally, I would like to thank my research advisor Dr. Karine Chesnel for providing all of the data I used in this analysis, and for her constant guidance – I couldn't have done this without her help.

Contents

List of Figures

Chapter 1

Introduction

The magnetic storage industry is constantly searching for new materials in order to satisfy ever increasing data storage density requirements [1]. Until recently, computer hard drive technology has been limited to using magnetic materials with in-plane magnetization geometry [2]. However, magnetic recording media where the domain topology points perpendicular to the substrate [3] has recently gained attention, due to its prospects of offering superior data storage density over existing technology. One such media possessing perpendicular magnetic domains is a [Co/Pd]IrMn thin film [4]. Our goal was to understand the magnetic memory properties of this material through directly analyzing the domain morphology against a wide array of applied magnetic fields.

We have probed the magnetic domain morphology of this thin film using soft X-ray coherent light. By this means we detected coherent X-ray scattering patterns related to the sample's magnetic domains. Coherently scattered X-rays reveal a scattering space representation of the local magnetic domain morphology in the thin film [5].

This technique of coherent soft X-ray resonant magnetic scattering (XRMS) produces results that are well suited to statistical analysis via cross-correlation metrol-

ogy [6]. We developed a suite of analysis programs in order to cross-correlate XRMS images. We used these cross-correlation results in order to analyze the amount of correlation between XRMS images acquired under varying external field conditions.

At certain applied fields, the number of field cycles appears to play only a minor role in effecting magnetic memory. This field strength dependence of magnetic memory is extremely important in understanding the magnetic memory behavior of the sample. A one-dimensional analysis shows how magnetic memory behaves with respect to field cycling and applied field by cross-correlating images acquired at identical and symmetrical field values. A two-dimensional analysis allows for studying magnetic memory behavior over every possible combination of applied fields.

Chapter 2

Outline of the Experiment

2.1 Sample Details

The sample we analyzed is a ferromagnetic (FM)/antiferromagnetic (AF) multilayer thin film with composition $([\mathrm{Co}(4\text{Å})/\mathrm{Pd}(7\text{Å})]_{12}\mathrm{IrMn}(24\text{Å}))_4$ (see Fig. 2.1). The FM component consists of a multilayer of cobalt (4Å thick) and palladium (7Å thick) layers. The AF component consists of a layer of IrMn alloy (24Å thick).

This sample exhibits perpendicular magnetic anisotropy leading to a striped domain morphology when the net magnetization is zero [4] (see Fig. 2.2). Uncompensated magnetic moments at the interface between the IrMn AF layer and the [Co/Pd] FM multilayer induces an exchange coupling effect [7] (see Fig. 2.3). This exchange coupling allows for control of the magnetic domain configuration in the [Co/Pd] multilayer [8].

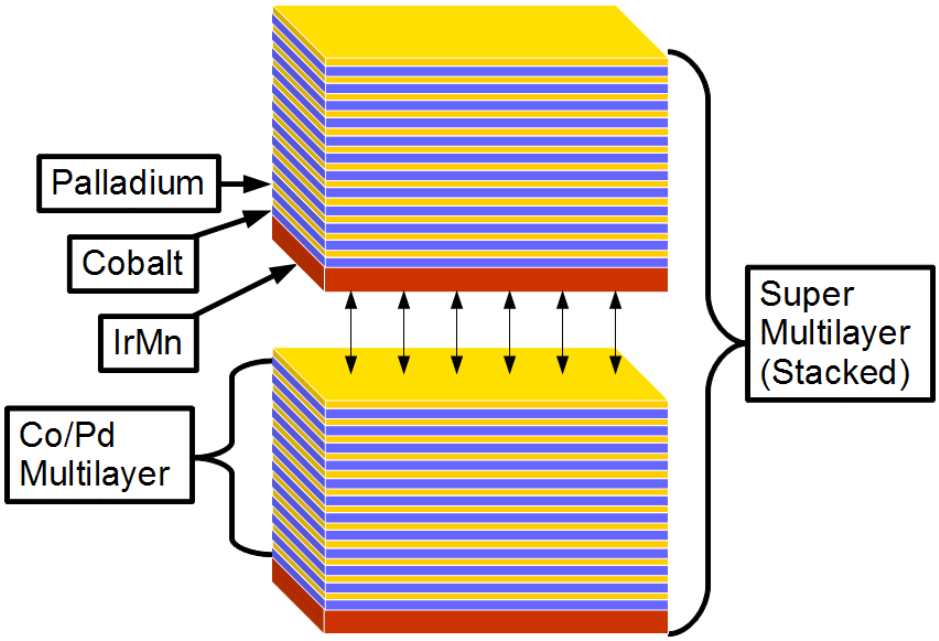

Figure 2.1 Sketch of a $([Co(4Å)/Pd(7Å)]_{12}IrMn(24Å))_4$ FM/AF multilayer thin film.

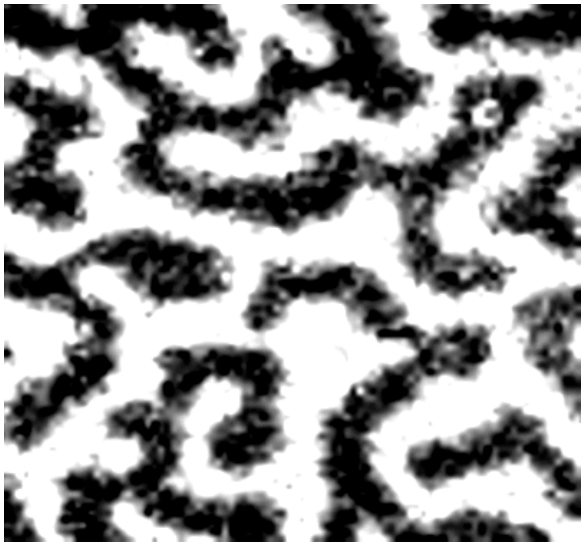

Figure 2.2 XRM image of magnetic domains in the magnetic thin film. Perpendicular anisotropy leads to a striped domain configuration when the net magnetization is zero. Image size is about 1μm x 1μm.

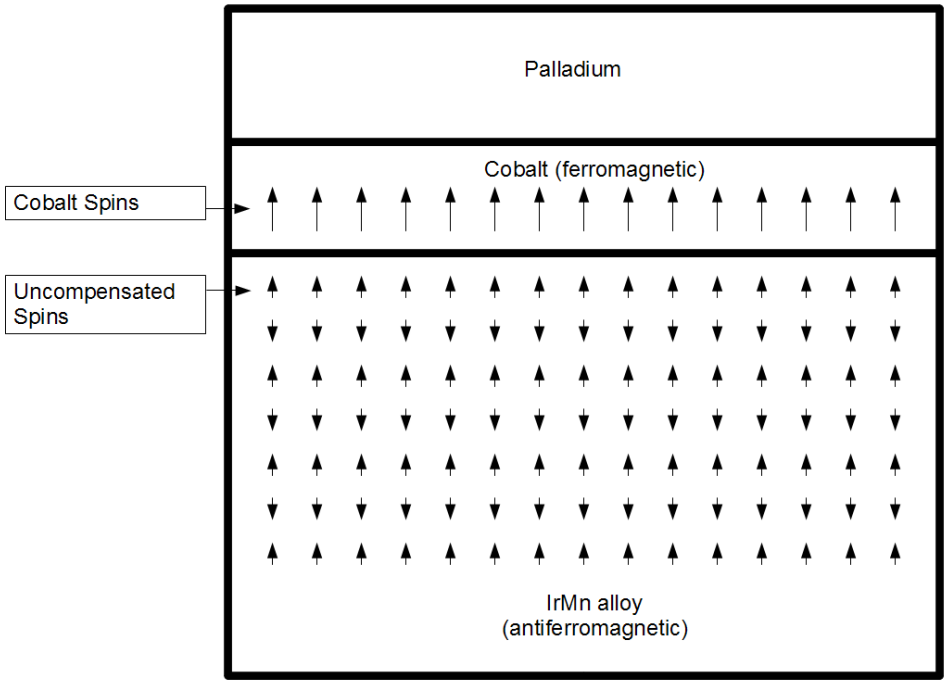

Figure 2.3 Schematical representation of the magnetic spins at the interface between an IrMn AF layer and a Co FM layer. Uncompensated spins are supposedly located on the IrMn side of the interface and are pointing upward in the sketch.

2.2 Our Motivation

The purpose of the experiment is to study specifically how the exchange coupling influences magnetic domain configuration in the FM multilayers. We desired to see if the exchange coupling would cause the magnetic domains to realign themselves in the same configuration after subjecting the sample to a variable magnetic field. By varying the field we could alter the magnetization of the sample, and hence, the magnetic domain configuration. The question was whether or not the uncompensated spins in the AF layer would influence the FM multilayer to return to a similar domain configuration after cycling the field multiple times. If we observed this effect it meant that exchange coupling could be used to induce magnetic memory.

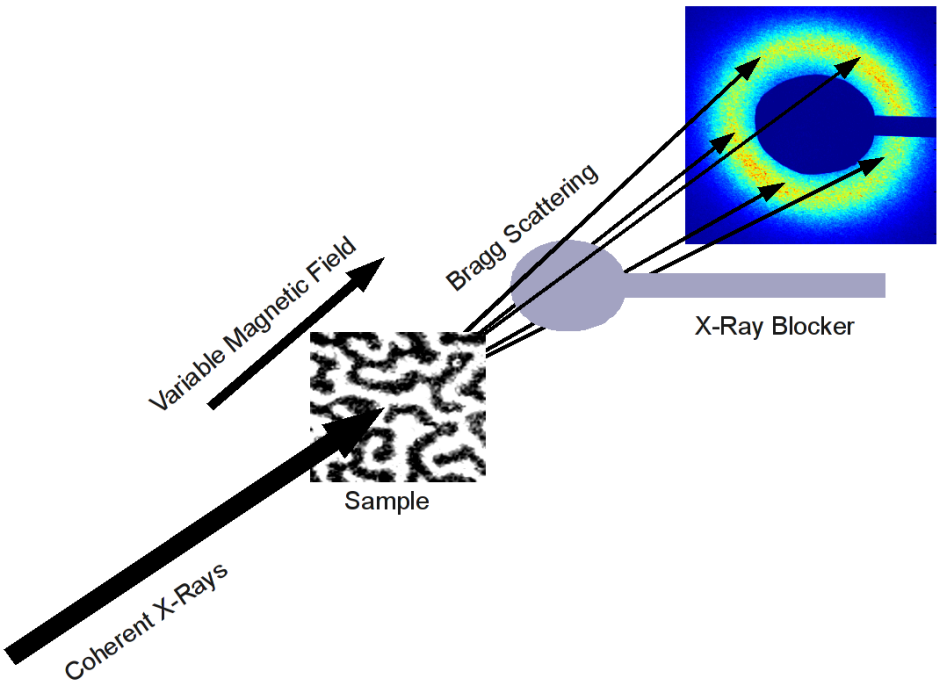

Figure 2.4 Experimental setup for detecting scattering patterns.

2.3 Experimental Procedures

Execution of the experiment required that the sample first be cooled to low temperatures in a zero external field (ZFC) state after initial demagnetization. Dropping below the blocking temperature ensured that magnetic domains arising from the uncompensated spins in the AF layer were frozen-in in a zero-net magnetization pattern (i.e. 50% of domains up, 50% of domains down) [4]. Applying ZFC to the sample also eliminated any macroscopic exchange bias [9, 10] within the sample.

We secured the sample within a variable magnetic field in transmission geometry, and illuminated it with coherent soft X-rays (see Fig. 2.4). In order to achieve magnetic contrast, the incident X-rays had an energy of 780eV, which coincides with the Co resonant L_3 edge. This resonance made possible the observation of scattering patterns generated by the magnetic domains [11]. We used a CCD camera in order

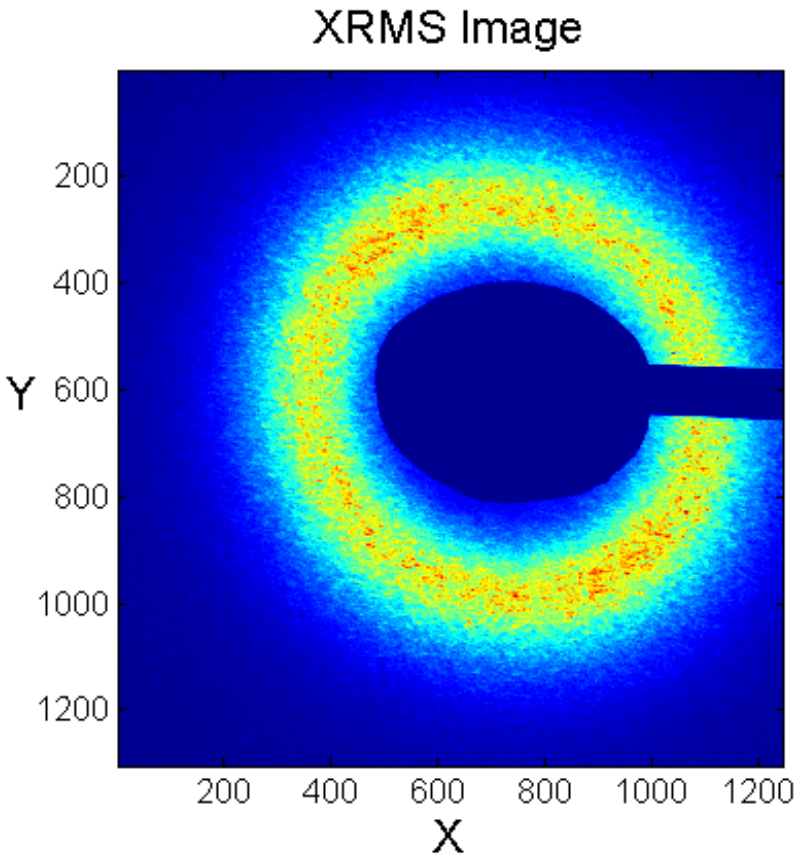

Figure 2.5 Typical XRMS image. The dark feature near the center of the XRMS ring is actually the shadow of an X-ray blocker used to protect the CCD camera from damage.

to detect XRMS images (see Fig. 2.5). The scattering patterns reveal (in scattering space) the local magnetic domain morphology in the sample [12].

The ring-like shape of the XRMS patterns reveals the general isotropy of the domain morphology. Because there is no preferential orientation in the domain morphology (see Fig. 2.2), the scattering pattern also presents an isotropic shape. The radius of the scattering ring is related to the period d of the magnetic domains according to the transmission geometry version of Bragg's law given in equation (2.1).

$$dsin\theta = n\lambda \tag{2.1}$$

Where λ is the wavelength of the incoming coherent X-ray light. Because the incoming

light had an energy of 780eV, this corresponds to a wavelength of about 1.60nm. Therefore, knowing the spacing between our sample and the CCD camera (1m), and knowing the radius of the scattering ring ($\sim$ 5.2mm) it is possible to estimate the period of the magnetic domains. In this case $d \sim 300$nm, which is approximately the same as what can be estimated visually from figure 2.2.

2.4 Method of Data Analysis

XRMS images are composed of the sum of two unique contributions: coherent scattering signal and incoherent scattering signal [8]. Coherent scattering signal manifests itself as speckle in the images. The speckle is surmounted upon a smooth envelope, which corresponds to the incoherent scattering signal (see Fig. 2.6). More on the importance of differentiating between coherent and incoherent scattering signal will be discussed in chapter 4.

By varying the applied magnetic field the morphology of the magnetic domains changes. We detected these changes as variations in the distribution of coherent XRMS scattering signal (see Fig. 2.7).

We used variations in speckle distribution in order to quantify magnetic memory in the sample. Statistical analysis via cross-correlation is the method we developed for measuring variations in speckle distribution [6]. By using cross-correlation we quantified the degree of similarity between different XRMS images. The degree of correlation corresponds to the similarity in the configuration of magnetic domains between two different states when images are taken. Therefore, we interpreted the degree of correlation to mean the amount of magnetic memory in the sample at a given external field strength.

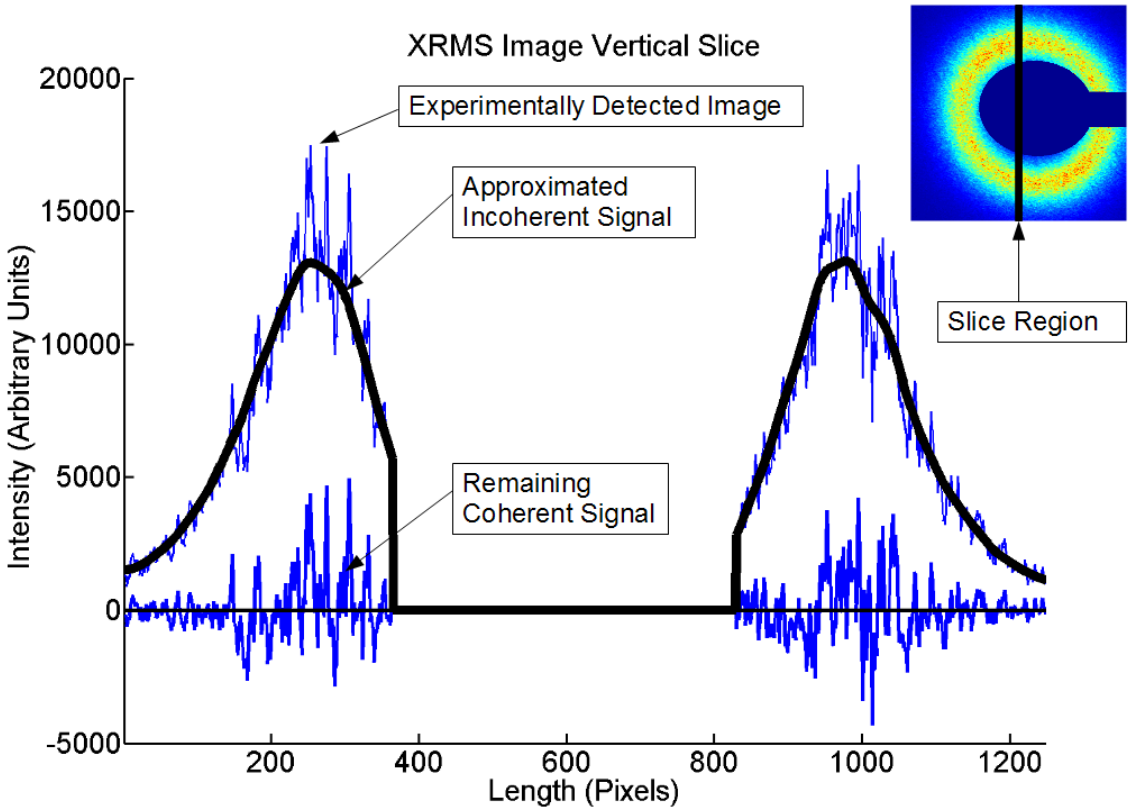

Figure 2.6 XRMS images are composed of coherent and incoherent scattering signal. This vertical slice through the center of an XRMS image shows the experimentally detected image, the computer approximated incoherent signal and the remaining coherent signal after separation from the experimentally detected image. The inset XRMS image contains a vertical stripe, which shows the approximate location for the vertical slice.

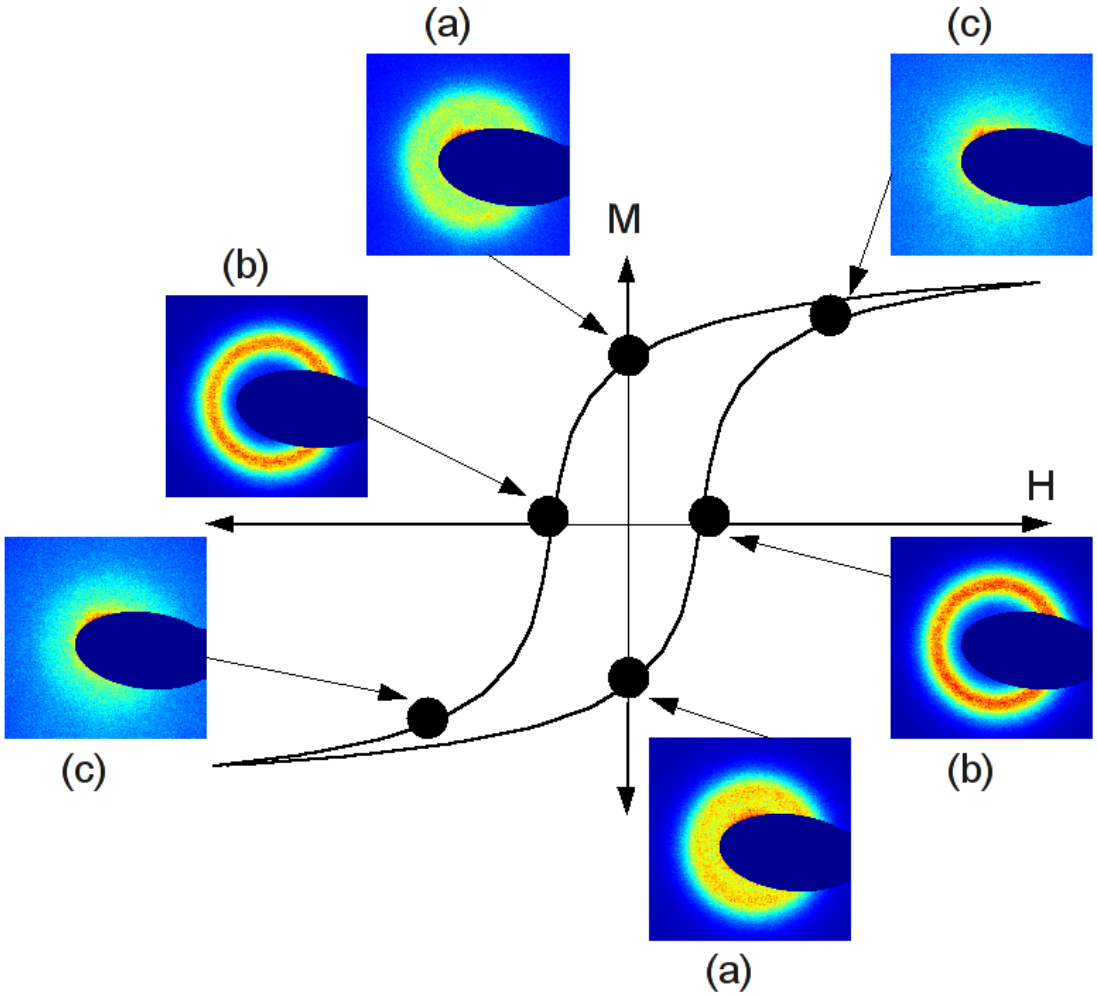

Figure 2.7 Hypothetical hysteresis curve for the sample with dots along the curve indicating approximately where several XRMS images were acquired. Changes in image morphology for images taken at different external fields (H) are apparent. (a) is an image taken at nucleation. (b) is an image taken in the coercive region. (c) is an image taken near saturation. These changes in image morphology were the direct result of alterations in the local domain morphology in the sample.

2.5 A Brief Explanation of Hysteresis

In the FM multilayers, the net magnetization of the sample does not follow a linear relationship to the applied field, but instead exhibits non-linear behavior. Additionally, FM material often exhibits hysteresis behavior. In order to organize the analysis of XRMS patterns, we divided the sample's hysteresis loop into two branches: the ascending branch and the descending branch as illustrated in figure 2.8. The definition of the ascending and descending branches is very important for determining a logical order for the analysis of XRMS images.

By quantifying magnetic memory over the entire range of the sample's hysteresis loop, we gained an understanding of the sample's magnetic memory behavior in three different regions: nucleation, the coercive region and saturation (see Fig. 2.8). On the ascending branch magnetic domains begin to nucleate when the external field (H) is greater than +37.5mT. The coercive region corresponds to the interval $+75mT < H < +300mT$. Saturation occurs approximately when $H > +400mT$.

If XRMS images are acquired after a complete demagnetization cycle (no remanent magnetization), then the first magnetization branch needs to be distinguished from the rest of the cycle. This is because the first magnetization branch does not follow the same path as the major loop of the sample's hysteresis curve (see Fig. 2.8). This detail needs to be carefully dealt with during analysis of magnetic memory. Measuring magnetic memory for images acquired during the first magnetization branch does not yield results that coincide well with predicted magnetic memory behaviors. Therefore, when creating graphs of results (chapters 6 and 7) we were careful as much as possible to only include that data which corresponds to the major loop of the sample's hysteresis curve.

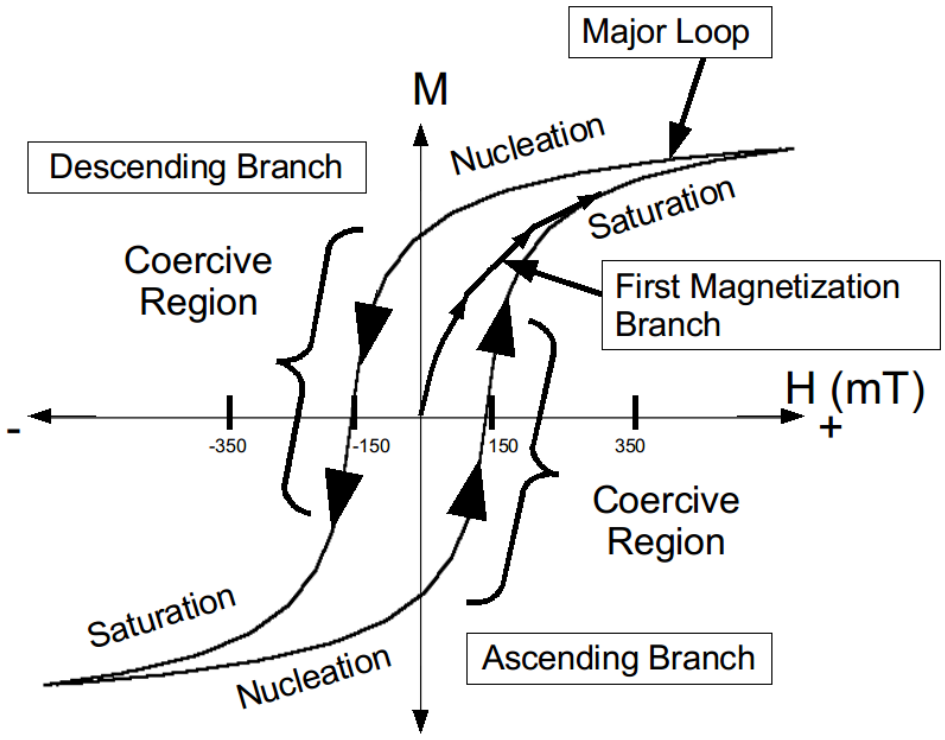

Figure 2.8 Sketch representing a typical hysteresis magnetization loop. Arrows along the hysteresis curve indicate the direction of traversal along the major loop of the hysteresis curve during external field (H) cycling. The ascending branch is traversed in the direction pointing from -H to +H. The descending branch is traversed in the direction from +H to -H. The different regions of the hysteresis loop are nucleation, the coercive region and saturation. Starting from a point of no remanent field (H,M) = (0,0) and applying a magnetic field (positive in this case) traverses the first magnetization branch. This branch does not match the major loop of the hysteresis curve. XRMS images acquired along the first magnetization branch; may therefore, not match images acquired at the same field value during subsequent field cycles.

Chapter 3

Cross-Correlation Technique

We implemented cross-correlation through two equivalent approaches. The first method cross-correlates two XRMS images by means of pixel-by-pixel multiplication. This method turned out to be a little computationally expensive, but it is very useful for illustrating the physical approach. The second method is almost identical to the first except it facilitates cross-correlation by using Fast Fourier Transforms (FFT). FFT based cross-correlation accomplishes the same task as pixel-by-pixel cross-correlation, but with significantly reduced processing time.

3.1 Pixel-by-Pixel Cross-Correlation Algorithm

The general formula for 2D pixel-by-pixel cross-correlation [13] is given in (3.1).

$$\mathcal{C}_{ab}(u,v) = a(x,y) \otimes b(-x,-y) = \int_{-\infty}^{\infty}\int_{-\infty}^{\infty} a(x,y) * b(u-x, v-y)\mathrm{d}x\mathrm{d}y. \qquad (3.1)$$

Where a and b are 2D matrices (XRMS images in this case). $\mathcal{C}_{ab}$ represents the cross-correlation of images a and b, and u and v are the translation indices that implement the $\otimes$ (convolution) operator. If a and b are identical images then the result of this operation is called an auto-correlation.

Our algorithmic implementation of operation (3.1) requires that the outside of image b be padded using periodic boundary conditions [14] (the right side of b is padded with pixels taken from the left side, the top is padded with pixels taken from the bottom, etc..). The width of the required padding is determined by the desired size of $\mathcal{C}_{ab}$. If the desired size of $\mathcal{C}_{ab}$ is MxM pixels then the width of padding that must be appended to each edge of b is $m = \frac{M-1}{2}$ pixels (therefore, the horizontal and vertical size of b increases by $M = 2 * m + 1$ pixels, due to the padding). This means that the total translation space available for convolving a over b (b remains stationary) ranges from $(u, v) = (-m, -m)$ to $(u, v) = (m, m)$. Therefore, the final size of $\mathcal{C}_{ab}$ is Mx$M = (2 * m + 1)$x$(2 * m + 1)$ (the addition of 1 covers $(u, v) = (0, 0)$).

As operation (3.1) translates a over b, overlapping pixels are multiplied and summed (see Fig. 3.1). The result of this summation is stored in a matrix, where the storage index (u, v) corresponds to the amount of translation. This matrix $\mathcal{C}_{ab}$ contains the cross-correlation result.

Total overlap between a and b occurs when $(u, v) = (0, 0)$ (see Fig. 3.1e). When total overlap occurs, (3.1) multiplies and sums every pixel contained in a and b. Therefore, in an auto-correlation ($\mathcal{C}_{aa}$) $(u, v) = (0, 0)$ always contains the maximum value, and usually so in the case of a cross-correlation $\mathcal{C}_{ab}$ (some offset in the maximum may occur in $\mathcal{C}_{ab}$).

The purpose of operation (3.1) is to quantify the degree of similarity between a and b using cross-correlation. In this case, the degree of similarity may be determined by analyzing the correlation peak (the central region of highest intensity in figure 3.2). This correlation peak corresponds to the average repeating speckle signal contained in XRMS images [8] (see Fig. 3.3). More on how the correlation peak relates to magnetic memory will be mentioned in chapter 5.

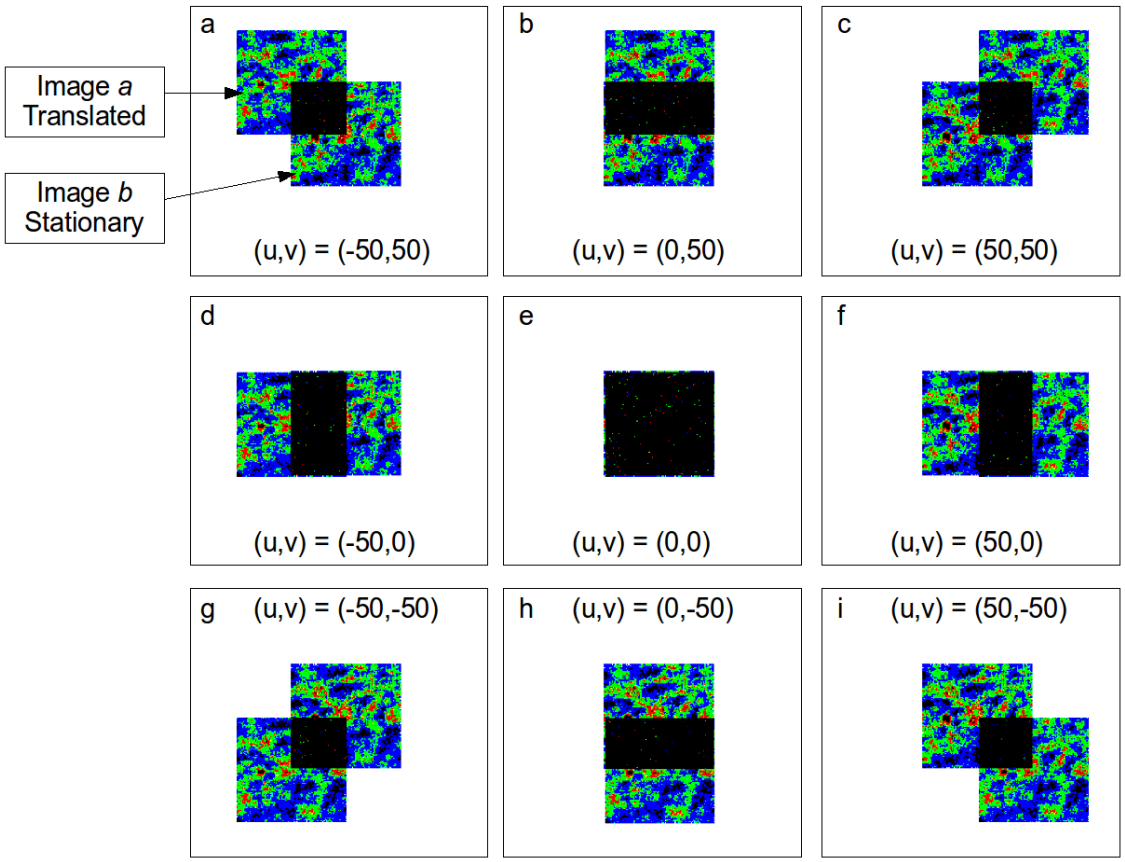

Figure 3.1 Illustration of pixel-by-pixel cross-correlation procedure. Desired size for $\mathcal{C}_{ab}$ is 201x201 pixels. Therefore, the padding width is set to $m = 100$ to allow total translation space of 201 pixels in either dimension. Overlaping regions have been pixel-by-pixel multiplied together, so they appear darker, due to much higher amplitude. Frame e corresponds to total overlap. The summation of overlapping pixels in frame e should yield the highest possible value located at $(u, v) = (0, 0)$ (the exact center) in $\mathcal{C}_{ab}$.

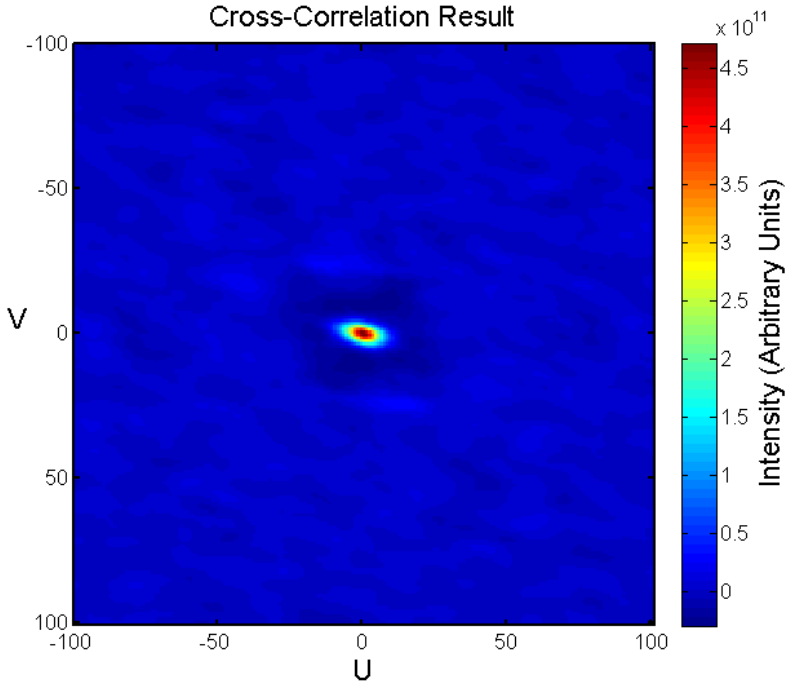

Figure 3.2 Cross-correlation result $\mathcal{C}_{ab}$. The correlation peak occurs around the central-most pixel where $(u, v) = (0, 0)$. The central-most pixel corresponds to total overlap, or figure 3.1e. Since $m = 100$, the size of $\mathcal{C}_{ab}$ is 201x201 pixels.

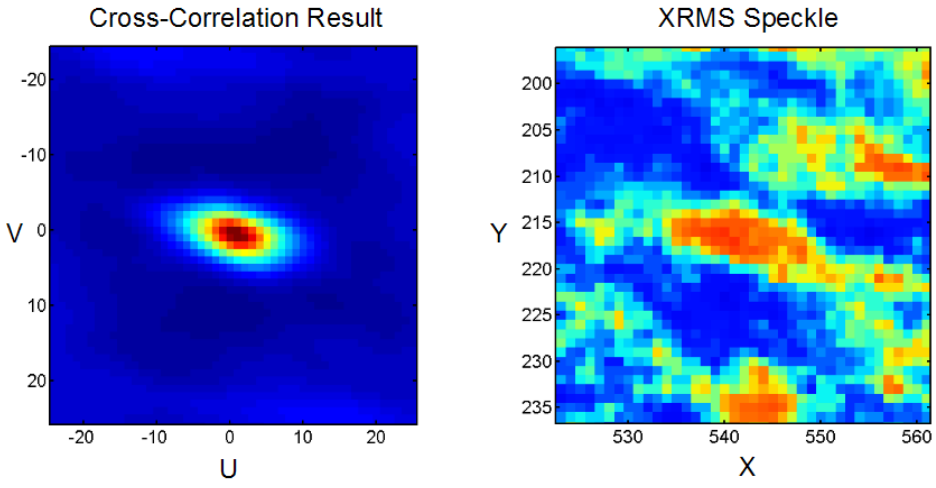

Figure 3.3 Left: closeup of the correlation peak in figure (3.2). Right: magnetic speckle contained in image a has a size, shape and orientation that is similar to the morphology of the correlation peak (average speckle).

The algorithm based on operation (3.1) has an order of complexity of $\mathcal{O}(N_x N_y M^2)$, where N_x is the horizontal size and N_y is the vertical size of images a and b, and $M = 2 * m + 1$ is the total width of horizontal/vertical padding appended to image b to allow translation of image a. For XRMS patterns where $N_x N_y = 1 * 10^6$ and $m = 40$ this algorithm should require $(1 * 10^6) * (2 * 40 + 1)^2 \sim 7 * 10^9$ calculations to finish output of $\mathcal{C}_{ab}$.

We measured this algorithm's performance at cross-correlating two XRMS images (size of images: 1304x1248, $m = 40$). This operation required about three minutes on an Intel EM64T processor (part of a compute node located in BYU's Fulton Supercomputing Laboratory) to complete. Therefore, cross correlating 100 images (10,000 cross-correlations) would take about three weeks (on a single processor). Parallel processing could have alleviated this problem. However, an FFT based cross-correlation algorithm offered considerable time-saving improvements regardless of parallelization.

3.2 FFT Based Cross-Correlation

FFT based cross-correlation produces results that are identical [15] to those obtained from operation (3.1). The expression for $\mathcal{C}_{ab}$ in terms of FFT [13] can be written as:

$$\mathcal{C}_{ab}(u, v) = \mathcal{F}^{-1}(\mathcal{F}(a(x, y)) * \mathcal{F}(b(-x, -y))). \tag{3.2}$$

Where $\mathcal{F}$ represents the two-dimensional Fourier transform operation, and $\mathcal{F}^{-1}$ represents the two-dimensional inverse Fourier transform operation. In this case the $*$ character represents pixel (as opposed to matrix) multiplication.

The technique requires that $b(x, y)$ first be rotated by 180 degrees in order to transform it into $b(-x, -y)$. Otherwise, operation (3.2) becomes the formula for convolution instead of cross-correlation. It is then necessary to take the Fourier transform of $a(x, y)$ and $b(-x, -y)$. Multiplying the Fourier transforms of $a(x, y)$ and

$b(-x,-y)$, and then taking the inverse Fourier transform of the product produces $\mathcal{C}_{ab}(u,v)$.

FFT based cross-correlation has an order of complexity of $\mathcal{O}(3N_xN_ylog_2(N_y))$ [16]. In order to cross-correlate two XRMS images ($N_x = 1248$, $N_y = 1304$) (3.2) should require $3 * 1248 * 1304 * log_2(1304) \sim 5.0 * 10^7$ calculations. The lower algorithmic complexity of operation (3.2) compared with operation (3.1) means that far fewer computations are required to produce the same result. On the same Intel EM64T processor as mentioned in the last paragraph of section 3.1 operation (3.2) required about one second to perform cross-correlation using the same a and b. This two order of magnitude reduction in running time made it possible to do necessary data analysis in a fraction of the amount of time that would have been required.

Chapter 4

Coherent Signal Extraction

4.1 Coherent vs. Incoherent Signal

XRMS images are the sum of two contributions: coherent signal corresponding to the local domain morphology, and incoherent signal corresponding to the long-scale configuration of magnetic domains [8]. These two types of signal are useful for different purposes. Specifically, the quantification of magnetic memory requires the isolation of the coherent contribution [8]. This requires separating the two contributions before or after performing cross-correlation. We refer to the procedure of removing incoherent signal before cross-correlation as pre-separation. Otherwise, we refer to the procedure of removing incoherent signal after cross-correlation as post-separation.

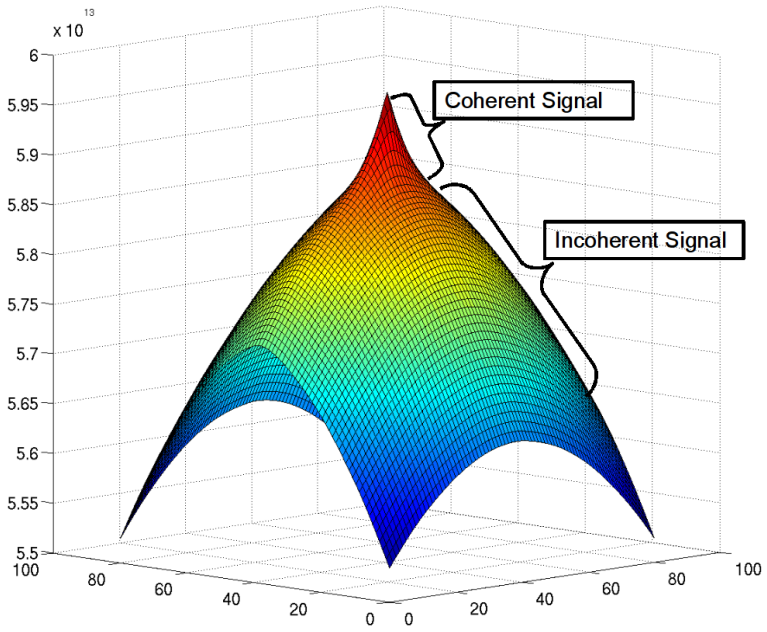

Figure 4.1 Cross-correlation result containing coherent and incoherent signal. Post-separation is now necessary in order to separate the two types of signal.

4.2 Post-Separation

Post-separation causes coherent and incoherent signal to exist together in the cross-correlation result ($\mathcal{C}_{ab}$). Cross-correlation of incoherent signal results in a bulbous shape. Cross-correlation of coherent signal results in a peak mounted on top of the bulbous envelope (see Fig. 4.1).

$\mathcal{C}_{ab}$ must have the coherent and incoherent contributions separated before it can be used to determine magnetic memory. This may be accomplished through fitting the bulbous background with a 2D weighted least-squares fit. A weighted fit makes it possible to avoid fitting the correlation peak. Including part of the correlation peak in the fit may result in a decrease in peak intensity, which could corrupt magnetic memory results. This weighted fit is then subtracted from $\mathcal{C}_{ab}$ in order to extract just the coherent contribution (see Fig. 4.2).

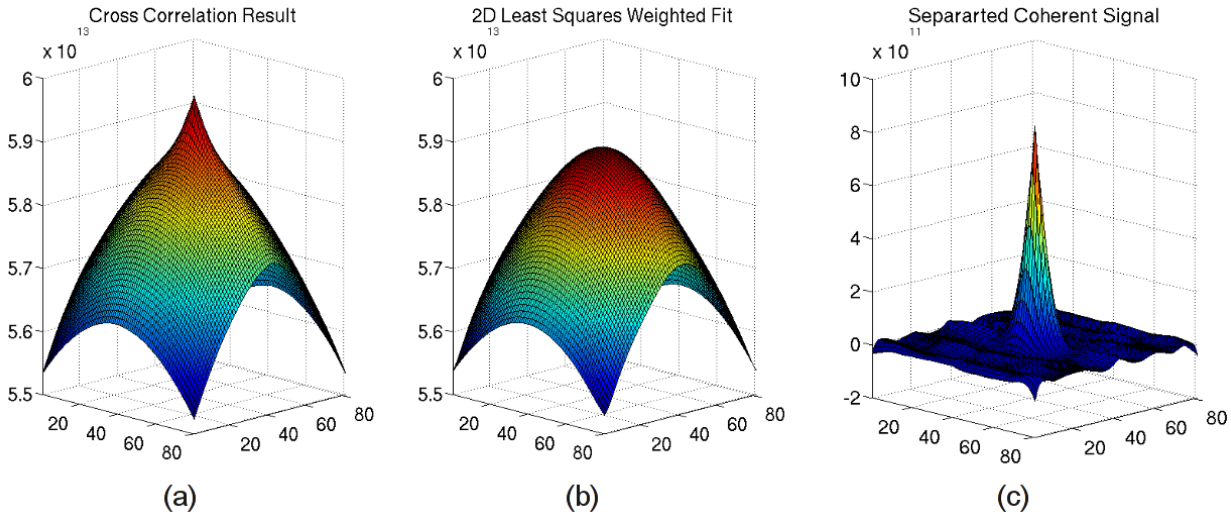

Figure 4.2 An illustration of the process of post-separating coherent from incoherent signal. (a) $\mathcal{C}_{ab}$ without pre-separation. (b) 2D least-squares weighted fit as an approximation of the incoherent signal. (c) After separation, only the coherent contribution remains.

However, adjusting the weighting accurately enough in order to avoid fitting the coherent contribution can be problematic. Particularly, in some cases the correlation peak is only slightly stronger in intensity than the incoherent envelope. In these cases it is usually very difficult if not impossible to avoid removing a portion of the coherent contribution during post-separation. Due to this difficulty, we developed pre-separation as an alternative.

4.3 Pre-Separation via 2D Least-Squares Fit

Pre-separation is possible through two-dimensional least-squares fitting of XRMS images. However, XRMS image data containing abrupt changes in magnitude presents some challenges for polynomial fitting. The large changes in magnitude present near the X-ray blocker induces deviations in the fit. Even by using very high degree polynomials it is still difficult to coax the fit around the blocker. Using very high degree

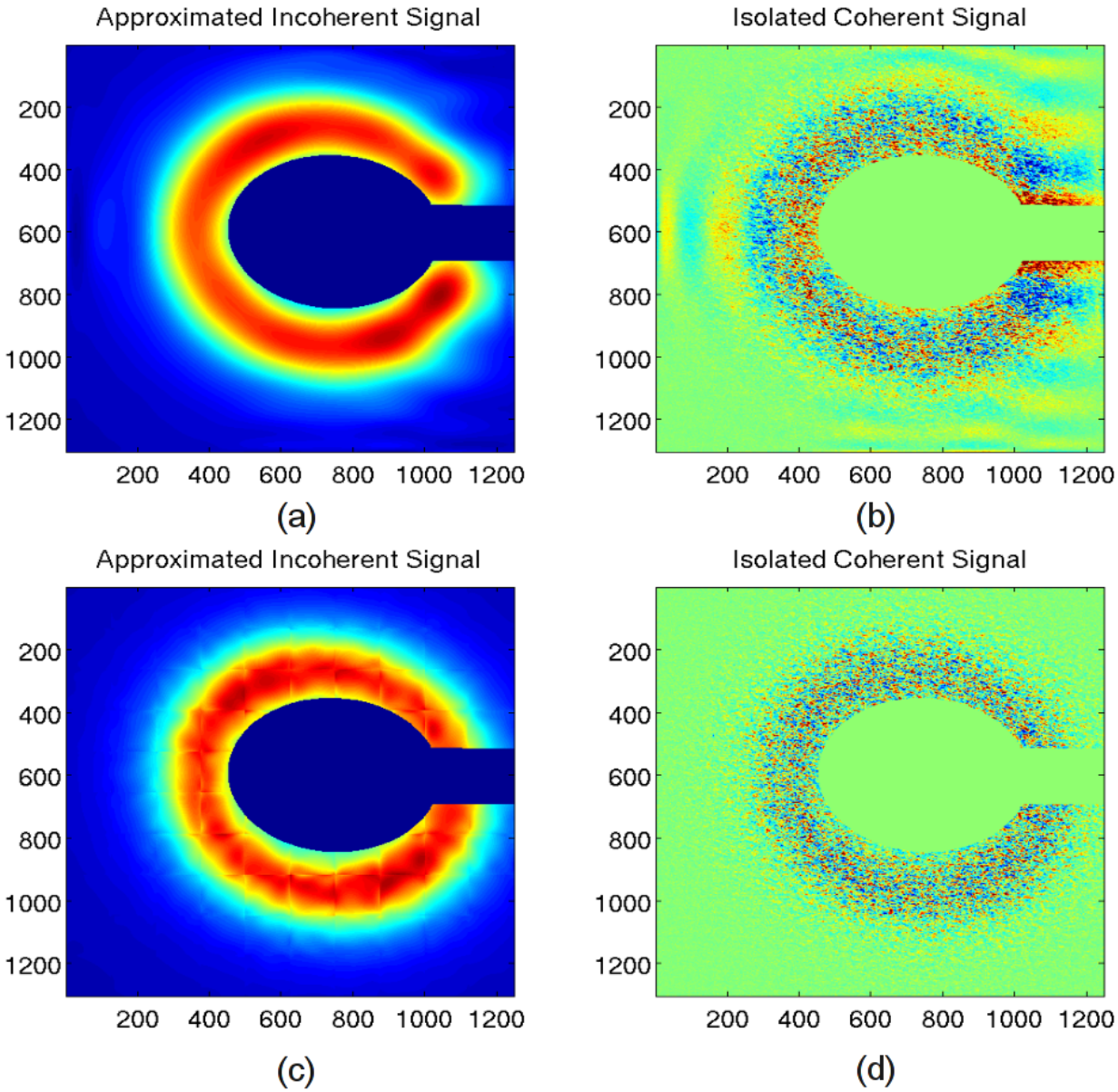

Figure 4.3 (a) Incoherent signal approximation through fitting of the entire XRMS image. Severe oscillation artifacts are present near the X-ray blocker and toward the upper and lower right corners of the image. (b) Isolated speckle signal produced by subtracting (a) from the original image. The speckle signal contains numerous oscillation artifacts particularly near the X-ray blocker. (c) Incoherent signal approximation via fitting multiple sectors individually and then reassembling each sector. This technique avoids oscillation artifacts, but introduces discontinuities between each sector. (d) Isolated speckle signal after subtracting (c) from the original image. Discontinuities between each sector are not easily visible in the figure, but are present.

polynomials also results in strong oscillation artifacts that alter the resulting fit (see Fig. 4.3a). This altered fit in turn produces artificial speckle results (see Fig. 4.3b), which manifests itself in the cross-correlation results.

It is possible to eliminate oscillation artifacts and satisfy significant changes in image magnitude by applying polynomial fitting by sections. This is accomplished by dividing each XRMS image into a grid (10x10 for example), fitting each of the grid sectors sequentially and then reassembling the product of this operation. This results in a collage of separately fitted sectors (see Fig. 4.3c). This collage is then subtracted from the XRMS data in an attempt to extract pure coherent signal. However, this technique results in numerous edge discontinuities between the borders of each sector. These discontinuities are propagated into the separated speckle (see Fig. 4.3d). This speckle corruption could effect the cross-correlation results. We therefore decided to try a pre-separation method that did not involve least squares fitting.

4.4 Pre-Separation via Pixel Averaging

Pre-separation is also possible by approximating the incoherent signal through pixel averaging. This method produces a smoothed version of the original image, which is an excellent approximation to the incoherent signal (see Fig. 4.4). If a_{inc} refers to the approximated incoherent signal obtained by smoothing image a, then it is possible to use a_{inc} to extract the coherent signal (a_{coh}) from image a through the matrix subtraction outlined in operation 4.1.

$$a_{coh} = a - a_{inc} \tag{4.1}$$

Pixel averaging does not introduce artificial oscillations or discontinuities into a_{coh}, as was the case with polynomial fitting. However, this technique requires determining

how many averaging passes are necessary before a suitable incoherent signal approximation is obtained. This required the creation of an algorithm to discontinue image averaging after a pre-set tolerance had been achieved.

A straight-forward implementation of pixel averaging uses a nested loop structure (double for-loop) in order to visit each pixel in an image sequentially. This algorithm produces smoothed images, but is time consuming. A somewhat more subtle implementation works row-by-row instead of pixel-by-pixel, and reduces time requirements considerably. However, like for cross-correlation an FFT based approach yields the fastest possible implementation. Each style of algorithm will be elaborated on.

4.4.1 Pixel-by-Pixel Averaging Algorithm

The pixel-by-pixel averaging algorithm sums all of the pixels contained within a 3x3 square, normalizes the sum and assigns the result to the central-most pixel according to operation (4.2).

$$a_{inc(p)}(x,y) = \frac{\sum_{i=x-1}^{x+1}\sum_{j=y-1}^{y+1} a_{inc(p-1)}(i,j)}{9}, \tag{4.2}$$

where $a_{inc(p)}$ is the approximated incoherent signal generated after p averaging passes, $a_{inc(p-1)}$ is the approximated incoherent signal generated during the previous averaging pass (if $p = 1$ then $a_{inc(p-1)} = a_{inc(0)} = a$, the original XRMS image). The algorithm smoothes $a_{inc(p-1)}$ by visiting all (x, y) contained in $a_{inc(p-1)}$ and performing operation (4.2).

In order to implement pixel-by-pixel averaging it is necessary to pad the edges of $a_{inc(p-1)}$ with pixels replicated from each of its borders [14]. Replicated border pixels allow the algorithm to function all the way out to the physical edges of $a_{inc(p-1)}$. The physical extent of $a_{inc(p-1)}$ after padding then extends from $(x, y) = (2, 2) \rightarrow (x, y) = (N_x - 1, N_y - 1)$, where N_xxN_y represents the size of $a_{inc(p-1)}$ after the

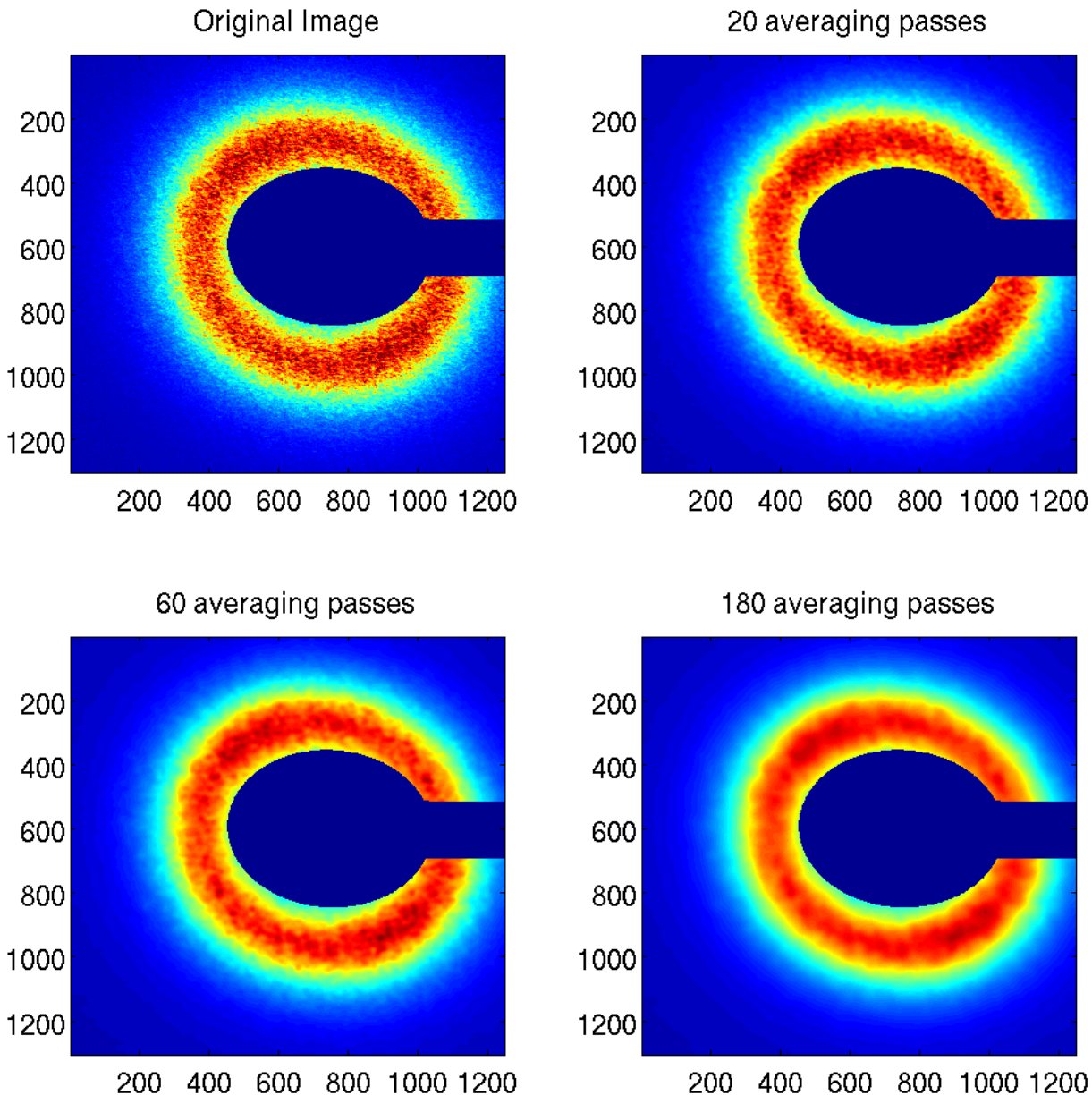

Figure 4.4 An example of how repeatedly averaging an image has a smoothing effect. The example given for 180 passes is close to what we expected an approximation to the incoherent signal to look like.

padding operation. After each averaging pass, we form $a_{inc(p)}$, which after employing operation (4.2) has a size of $(N_x - 2)$x$(N_y - 2)$ (we define x and y in operation (4.2) only within the physical extents of image $a_{inc(p-1)}$ in order to satisfy the boundaries). Therefore, during each averaging pass $a_{inc(p-1)}$ has a size of N_xxN_y, due to padding; whereas, $a_{inc(p)}$ has a size of $(N_x - 2)$x$(N_y - 2)$, due to the boundary conditions.

The order of complexity for this algorithm is $\mathcal{O}(9N_xN_yP)$, where P is the number of averaging passes. However, this algorithm uses nested loops, which our computational environment is not efficient at processing. Therefore, the actual order of complexity within our computational environment may be substantially different from what we have described here.

Approximating the incoherent signal with operation (4.2) requires about 200 averaging passes. On an Intel EM64T processor each averaging pass requires about five seconds (size of image: 1304x1248). Therefore, about 16 to 17 minutes of compute time per pre-separation operation is typical. A slightly different approach working row-by-row instead of pixel-by-pixel improved running times by greater than an order of magnitude.

4.4.2 Row-by-Row Averaging Algorithm

Row-by-row averaging duplicates the output of operation (4.2), but significantly more quickly. It is accomplished by using a loop to iterate over each row of $a_{inc(p-1)}$ from $y = 2$ to $y = N_y - 1$. The subtilty is to collapse groups of 3 rows of pixels into a vector (V_{sum}) containing the column-wise sum of the 3 rows. This operation is performed according to equation (4.3) and results in V_{sum} with length equal to N_x (the horizontal length of $a_{inc(p-1)}$ after the padding operation discussed in section 4.4.1).

$$V_{sum}(v_x) = a_{inc(p-1)}(v_x, y-1) + a_{inc(p-1)}(v_x, y) + a_{inc(p-1)}(v_x, y+1), \tag{4.3}$$

where $y \in [2...N_y - 1]$ and v_x is an indexing vector of length N_x used to quickly extract x-dimension indices contained in $a_{inc(p-1)}$ for the summation.

We defined three additional indexing vectors: $v_{x1} = [1, 2, 3, ..., N_x - 2]$, $v_{x2} = [2, 3, 4, ..., N_x - 1]$ and $v_{x3} = [3, 4, 5, ..., N_x]$ in order to create a shift for the final summation. The algorithm uses v_{x1}, v_{x2} and v_{x3} in order to index V_{sum} at the appropriate locations for duplicating the output of operation (4.2). The algorithm sums the values contained in V_{sum} at locations indexed by v_{x1}, v_{x2} and v_{x3} in order to form a new summation vector. This vector is then normalized and inserted into $a_{inc(p)}$ according to operation (4.4).

$$a_{inc(p)}(v_{x2}, y) = \frac{V_{sum}(v_{x1}) + V_{sum}(v_{x2}) + V_{sum}(v_{x3})}{9}, \tag{4.4}$$

where again $y \in [2...N_y - 1]$. The algorithm uses v_{x2} as the indexing vector to determine the x-indices for insertion of averaged values into $a_{inc(p)}$.

The speed of row-by-row averaging is greater than pixel-by-pixel averaging, because of the replacement of the nested loop structure with indexing vectors v_{x1}, v_{x2} and v_{x3}. Row-by-row averaging decreases the running time from five seconds to about 200 milliseconds per averaging pass (size of image: 1304x1248), even though the order of complexity is still $\mathcal{O}(9N_xN_yP)$. The key was to code the averaging algorithm in such a way that our computational environment is able to work most efficiently. This makes it possible to average a to appropriate levels in less than 40 seconds. However, an FFT based approach increased speed by more than double.

4.4.3 FFT Based Averaging Algorithm

The theory behind using FFTs for smoothing $a_{inc(p-1)}$ requires the definition of a smoothing function f [15]. This smoothing function f is a matrix, and is called a Point Spread Function (PSF). This PSF is Fourier transformed and multiplied with

the Fourier transform of $a_{inc(p-1)}$ according to (4.5).

$$a_{inc(p)} = \mathcal{F}^{-1}(\mathcal{F}(a_{inc(p-1)}) * \mathcal{F}(f)), \tag{4.5}$$

where the multiplication ($*$) is pixel-wise and not matrix multiplication. Operation (4.5) appears very similar to operation (3.2) with the exception that matrix f is not rotated before taking its Fourier transform. The necessity of rotating is a key difference between cross-correlation and convolution. Multiplication of $a_{inc(p-1)}$ by the non-rotated matrix f in Fourier space results in the convolution of matrix f over $a_{inc(p-1)}$, which produces the smoothing effect [15].

In order for matrix f to duplicate the output of operations (4.2) and (4.4) it must be defined as a normalized ($\sum f = 1$), flat matrix (size 3x3 in this case) [15]. Otherwise, if matrix f is not normalized, the average amplitude of $a_{inc(p)}$ is steadily altered after each averaging pass.

Use of operation (4.5) decreased the running time to about 75 milliseconds per averaging pass (size of image: 1304x1248). Therefore, approximating incoherent signal usually required about 15 seconds per image. The order of complexity is $\mathcal{O}(3N_xN_ylog_2(N_y)P)$ [16]. This order of complexity is somewhat worse than for operations (4.2) and (4.4). However, the higher speed of operation (4.5) is due to the optimized FFT package we used in implementing it.

4.5 Isolating Pure Coherent Signal

Approximating incoherent signal using operation (4.2), (4.4) or (4.5) requires a different number of averaging passes depending on the image. Developing an algorithm that determines when sufficient averaging has been achieved allowed us to save a tremendous amount of time, because we do not have to manually process each image.

Motivation to develop such an algorithm was based on experience gained from over-averaging and under-averaging images. If an image is over-averaged then this results in under-estimation of the incoherent signal (see Fig. 4.5). When this occurs, remnants of the incoherent signal remain in the isolated speckle. Conversely, if the image is under-averaged, then it results in speckle corruption during separation (see Fig. 4.6). Cross-correlation of under-averaged or over-averaged images yields questionable magnetic memory results.

The algorithm checks for convergence to an empirically determined tolerance (τ) by repeatedly measuring the range ($R_{coh}(p)$) of $a_{coh(p)}$ (the coherent signal approximation after p averaging passes) after every averaging pass (p). Every time the algorithm employs operation (4.5) it takes as input $a_{inc(p-1)}$, the incoherent signal approximation for image a after $p-1$ averaging passes, to form $a_{inc(p)}$. It then uses operation (4.6) in order to examine $R_{coh}(p)$ (see Fig. 4.7).

$$R_{coh}(p) = max(a_{coh(p)}) - min(a_{coh(p)}). \tag{4.6}$$

The algorithm takes numerical derivatives of $R_{coh}(p)$ using the centered finite difference 2nd derivative formula:

$$\frac{d^2 R_{coh}(p)}{dp^2} = \frac{R_{coh}(p+1) - 2R_{coh}(p) + R_{coh}(p-1)}{1^2}. \tag{4.7}$$

The 2nd derivative of $R_{coh}(p)$ provides a break condition in order to discontinue image averaging as soon as $\frac{d^2 R_{coh}(p)}{dp^2} < \tau$ (see Fig. 4.8).

Through experimentation we determined an optimal range for τ to be from 0.01 to 0.05. Setting τ to values far oustide this range usually results in under or over averaged output. Using τ with operation (4.7) to control the break condition for operation (4.5) is a very effective means of accurately approximating incoherent signal (see Fig. 4.9 and Fig. 4.10).

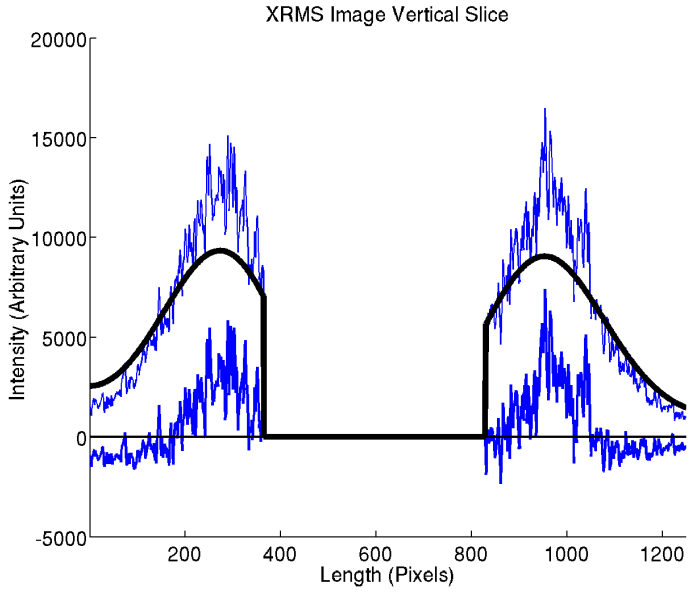

Figure 4.5 Example of over-averaging. The incoherent signal approximation is no longer an accurate fit of the incoherent signal. Part of the incoherent signal is still present in the separated coherent signal.

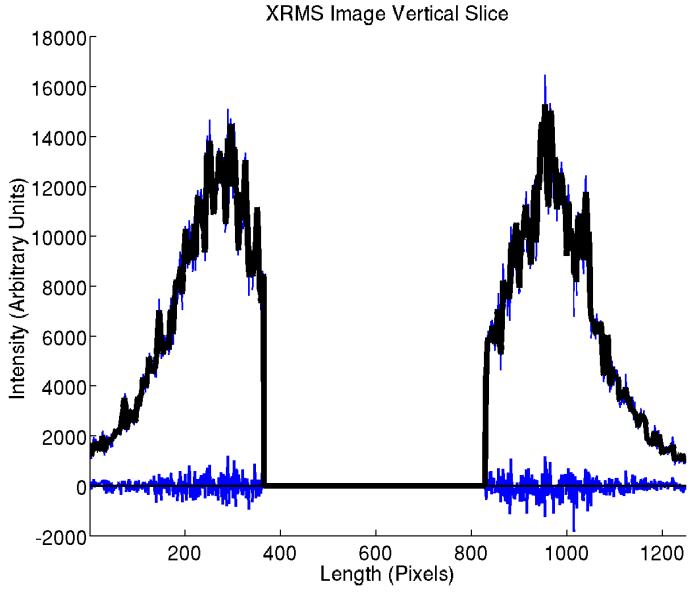

Figure 4.6 Example of under-averaging. Most of the separated coherent signal is lost, due to insufficient smoothing of the original image.

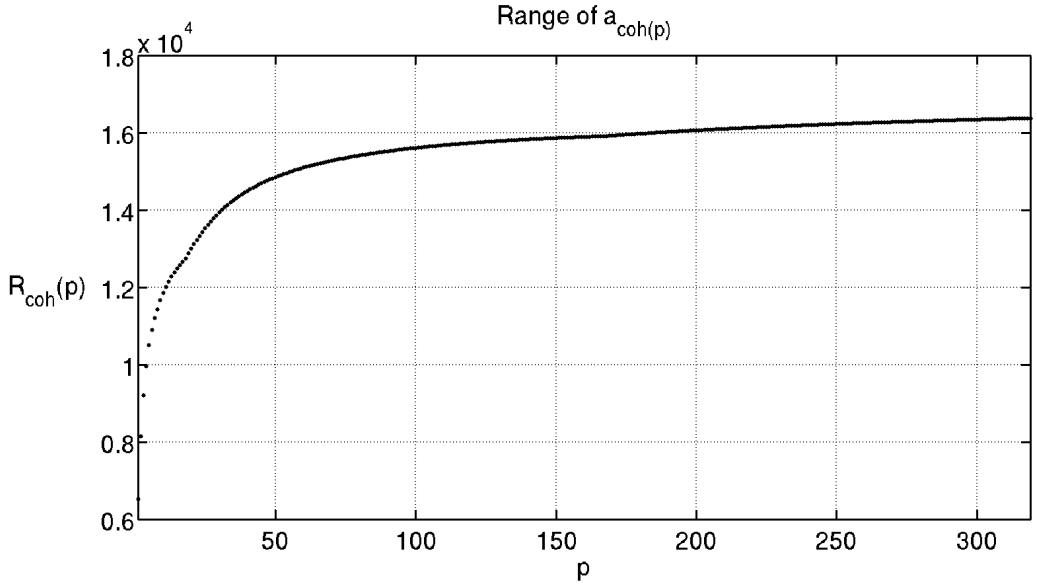

Figure 4.7 The range of $a_{coh(p)}$ increases rapidly with the first several averaging passes. However, as $a_{inc(p)}$ becomes steadily smoother, the increase in range of $a_{coh(p)}$ gradually slows down ($\frac{d^2 R_{coh}(p)}{dp^2} \rightarrow \tau$). Eventually, additional averaging passes have very little effect on the range of $a_{coh(p)}$, and it is appropriate to discontinue averaging.

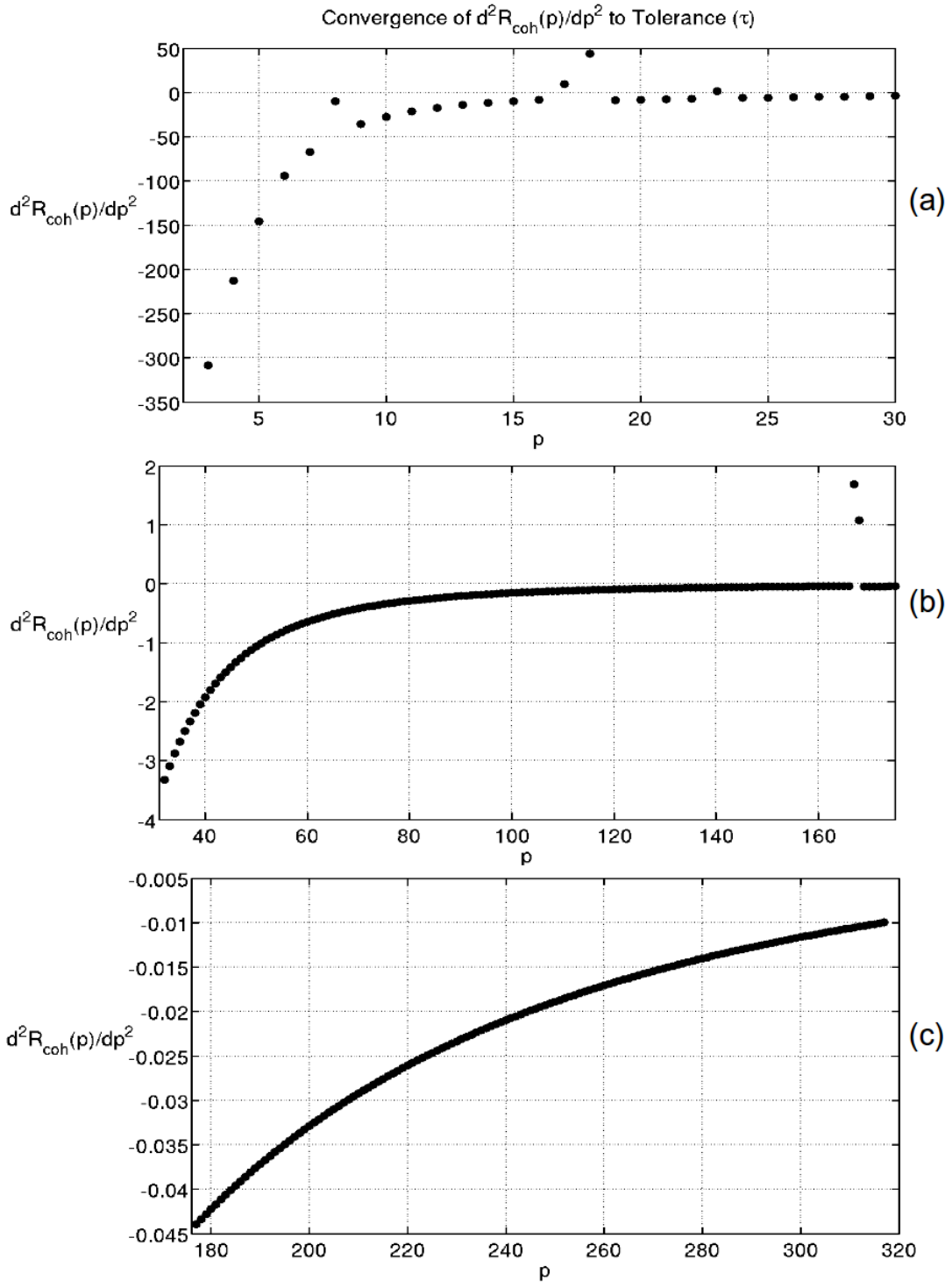

Figure 4.8 Example of convergence of $\frac{d^2R_{coh}(p)}{dp^2}$ to tolerance ($\tau = 0.01$) for the same $R_{coh}(p)$ shown in figure (4.7). $\frac{d^2R_{coh}(p)}{dp^2}$ converged after 317 averaging passes. (a) passes 3 through 35, (b) passes 36 through 175, (c) passes 176 through 317. Each graph has a different vertical scale to emphasize rate of convergence.

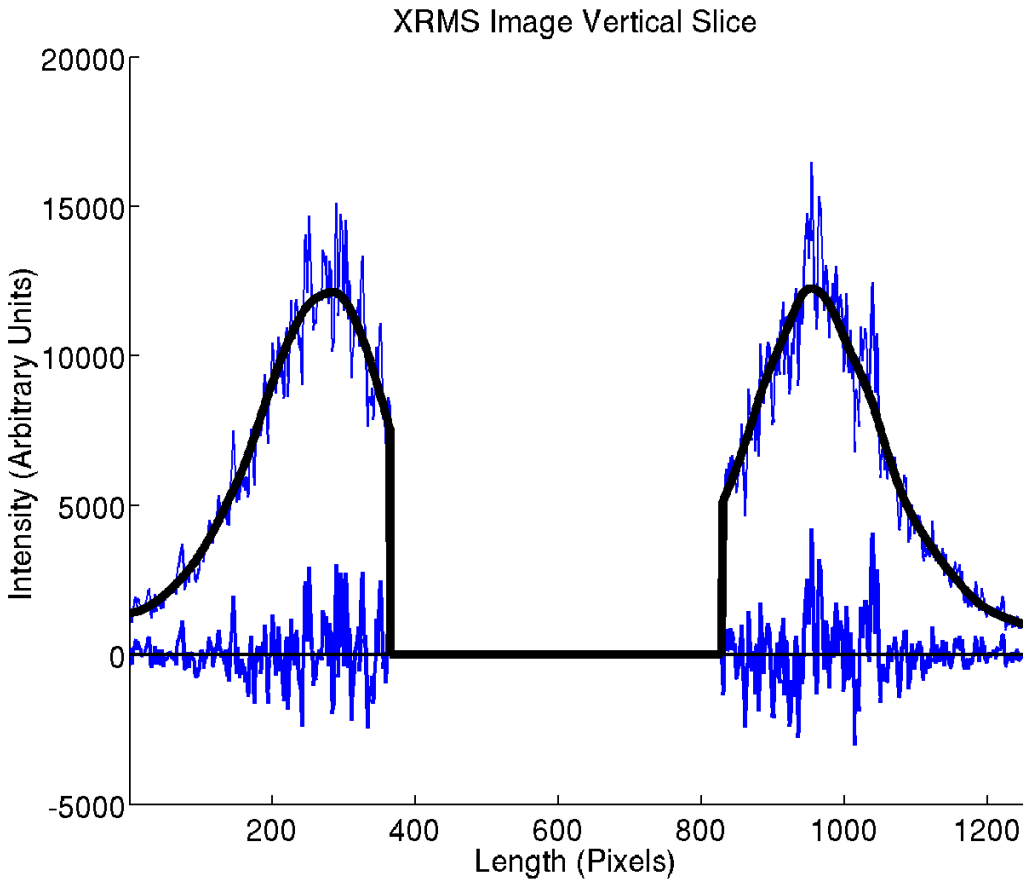

Figure 4.9 Example of appropriate averaging using operation (4.7). τ was set to 0.01, which required about 300 averaging passes in order to converge. The difference between the separated coherent signal in this figure as opposed to figure 4.5 and figure 4.6 is evident.

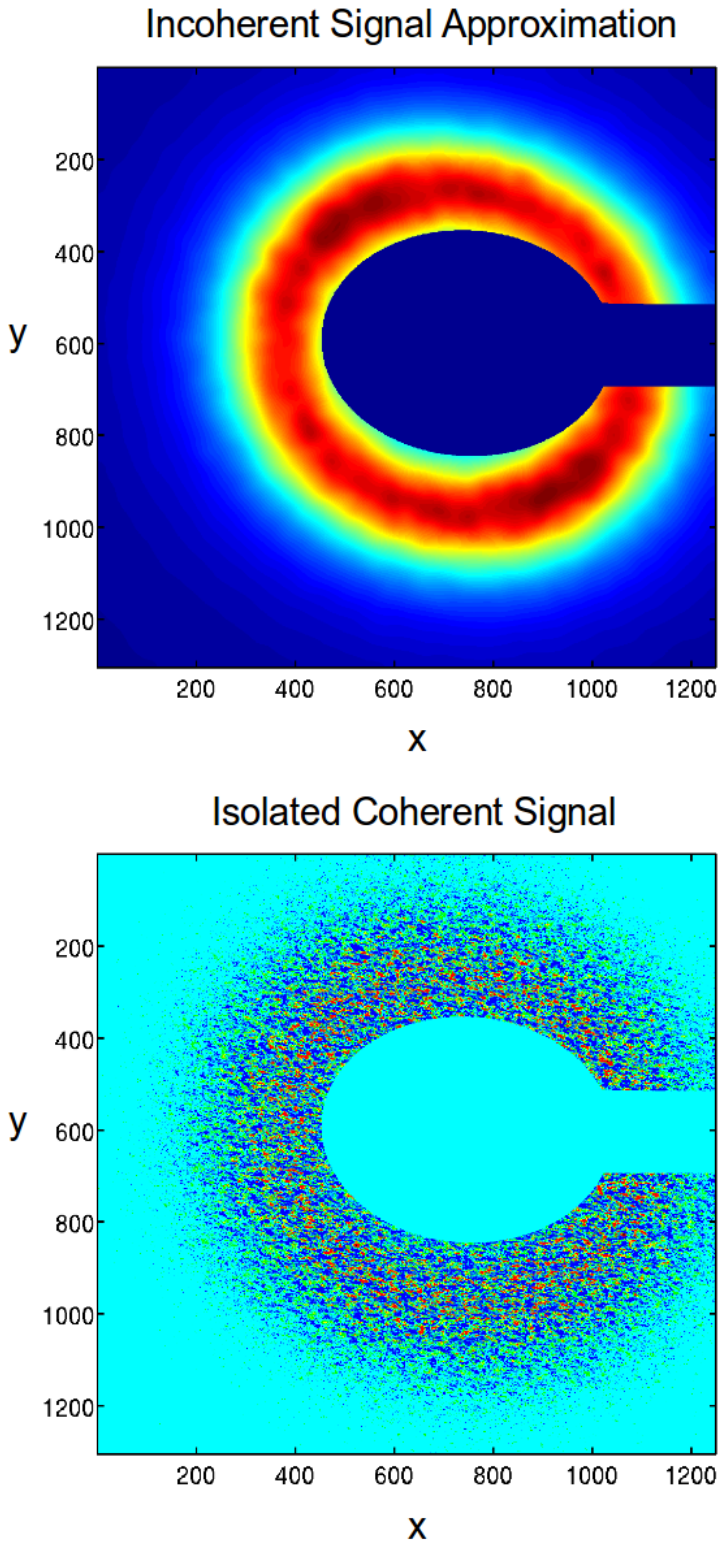

Figure 4.10 Example of appropriate levels of averaging showing final coherent and incoherent signal approximations. ($\tau = 0.01$)

Chapter 5

Quantification of Magnetic Memory

5.1 Degree of Coherence β

XRMS images differ in amplitude of coherent signal. Higher amplitude coherent signal allows a clearer distinction between the coherent and incoherent contributions during pre-separation. Greater accuracy in isolating coherent signal produces magnetic memory results that match more closely with predicted behaviors. Therefore, quantifying quality of speckle is an important step in interpreting magnetic memory results.

Quantifying the quality of speckle is accomplished by calculating the degree of coherence β. Degree of coherence may be calculated [17] by using the normalized standard deviation of the speckle pattern, which can be written as equation (5.1).

$$\beta = \sqrt{\frac{\sum_{x,y}(a(x,y) - a_{inc}(x,y))^2}{\sum_{x,y} a_{inc}(x,y)^2}} \tag{5.1}$$

Where $a(x,y)$ is the original image, $a_{inc}(x,y)$ is the approximated incoherent signal and $a(x,y) - a_{inc}(x,y)$ is just the isolated coherent signal $a_{coh}(x,y)$ obtained from using

operation (4.1). After taking advantage of operation (4.1), equation (5.1) becomes equation (5.2).

$$\beta = \sqrt{\frac{\sum_{x,y} a_{coh}(x,y)^2}{\sum_{x,y} a_{inc}(x,y)^2}} \tag{5.2}$$

Since β is a normalized quantity, valid values range between 0 and 1. If $\beta = 1$ then image a consists entirely of coherent signal. However, typical values for β for the XRMS images we acquired ranges from about 7.5% to about 20% meaning that the majority of our images consist of incoherent signal. Regardless of this, we were still successful at extracting the coherent signal from the images, so it was still possible to measure the degree of correlation between XRMS images with very good accuracy.

5.2 Degree of Correlation ρ

As mentioned in chapter 3, the correlation peak in a cross-correlation result $\mathcal{C}_{ab}$ contains information regarding magnetic memory in the sample. Quantification of magnetic memory is performed by computing the quantity ρ:

$$\rho = \frac{\sum \mathcal{C}_{ab}(u,v)}{\sqrt{\sum \mathcal{C}_{aa}(u,v) \sum \mathcal{C}_{bb}(u,v)}}. \tag{5.3}$$

ρ is the coefficient of correlation between images a and b [8]. The purpose of dividing by the square root of the product of the auto-correlations $\mathcal{C}_{aa}$ and $\mathcal{C}_{bb}$ is to normalize ρ. Valid values for ρ occur between 0 and 1, where 0 indicates absolutely no memory and 1 indicates total memory. By using equation (5.3) on an auto-correlation result ($a = b$) the resulting ρ is 1.

The differences in morphology between $\mathcal{C}_{aa}$ and $\mathcal{C}_{ab}$ is important to equation (5.3). $\mathcal{C}_{aa}$ always contains a well-defined correlation peak (see Fig. 5.1). However, $\mathcal{C}_{ab}$'s correlation peak is dependent on the similarity of a and b (see Fig. 5.2). Integrating $\mathcal{C}_{aa}$ usually produces a larger value than integrating $\mathcal{C}_{ab}$.

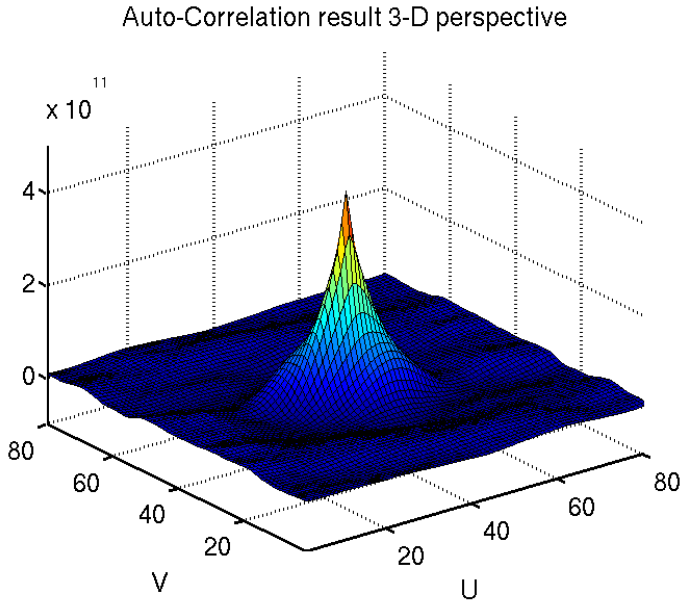

Figure 5.1 A typical auto-correlation result ($\mathcal{C}_{aa}$).

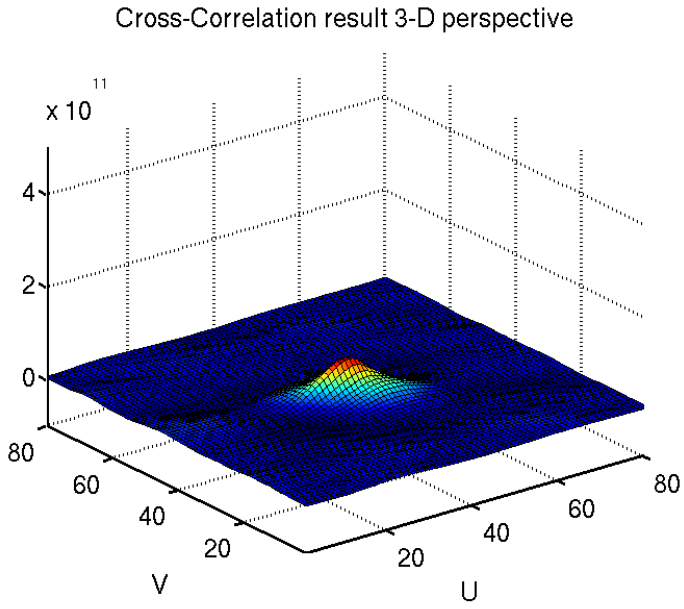

Figure 5.2 A typical cross-correlation result ($\mathcal{C}_{ab}$). There is a dramatic difference in the size of the correlation peak compared with $\mathcal{C}_{aa}$ in figure 5.1. Vertical axes on both figures are equal.

5.3 Integration Procedure

Before integrating $\mathcal{C}_{ab}$ it is necessary to isolate an appropriate region for integration. FFT based cross-correlation produces results with the same size as the input images (see Fig. 5.3). However, only the small region centered around the correlation peak is useful for determining magnetic memory. The correlation peak is always located at the center of $\mathcal{C}_{aa}$, but in the case of $\mathcal{C}_{ab}$ the correlation peak may be slightly offset from $(u, v) = (0, 0)$.

Because the correlation peak in $\mathcal{C}_{ab}$ is not always located exactly at $(u, v) = (0, 0)$, it is necessary to crop $\mathcal{C}_{ab}$ around its maximum value. The maximum value almost always coincides with location of the correlation peak. After cropping, the correlation peak contained in $\mathcal{C}_{ab}$ is essentially relocated to the matrix index where $(u, v) = (0, 0)$. The size of $\mathcal{C}_{ab}$ after cropping is chosen arbitrarily to be MxM = 81x81 pixels. This size is sufficient such that all of the correlation peak is always contained within this square matrix. Also, this size is small enough that storing several hundred thousand $\mathcal{C}_{ab}$ matrices does not require unreasonable storage capacity.

Even with $\mathcal{C}_{ab}$ cropped and the correlation peak centered at $(u, v) = (0, 0)$, it is still necessary to define a region within $\mathcal{C}_{ab}$ for integration. Integrating over a rectangular region is not optimal, because the correlation peak is elliptic. Therefore, we fit an ellipse around the correlation peak in order to extract only the peak and not any surrounding correlation data (see Fig. 5.4). Typical parameters for a fitting ellipse correspond to a semi-major axis of 20 pixels and a semi-minor axis of 16 pixels. This size is usually sufficient to capture the entire correlation peak for most $\mathcal{C}_{ab}$. With the correlation peak isolated equation (5.3) may be used in order to determine magnetic memory.

We developed a procedure for rapidly quantifying ρ for tens of thousands of cross-correlation results. We applied this procedure to analyze several sets of XRMS image data. By using the output of this procedure, we created one-dimensional graphs (chapter 6) and two-dimensional maps (chapter 7) of magnetic memory. Our analysis successfully characterizes the effects of exchange coupling on magnetic memory behavior in our sample.

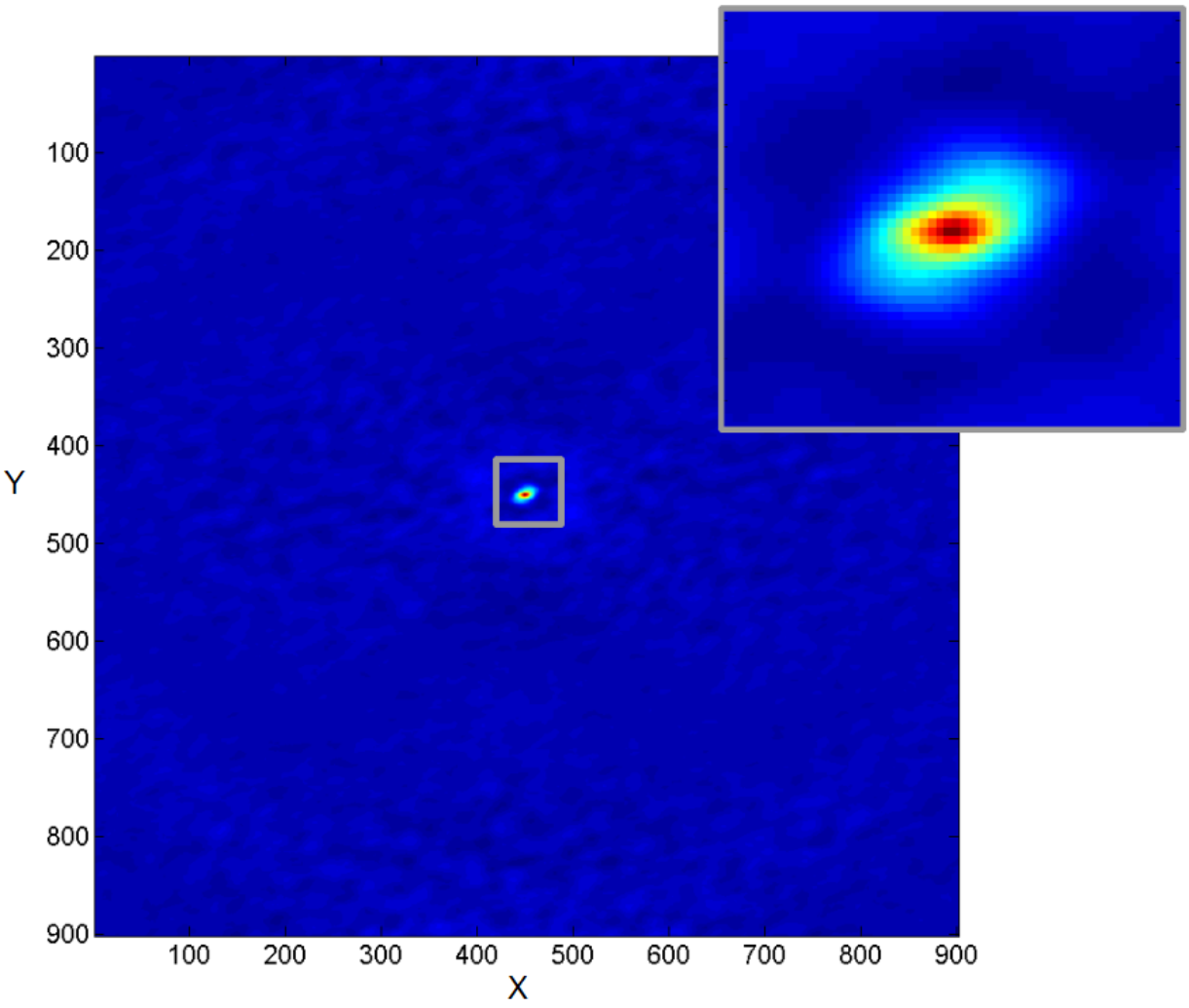

Figure 5.3 Full cross-correlation pattern resulting from using operation 3.2. Size is 901x901 pixels, because a and b are both 901x901 pixels. Inset: cropped region near the center of the image containing the correlation peak, used for determining magnetic memory.

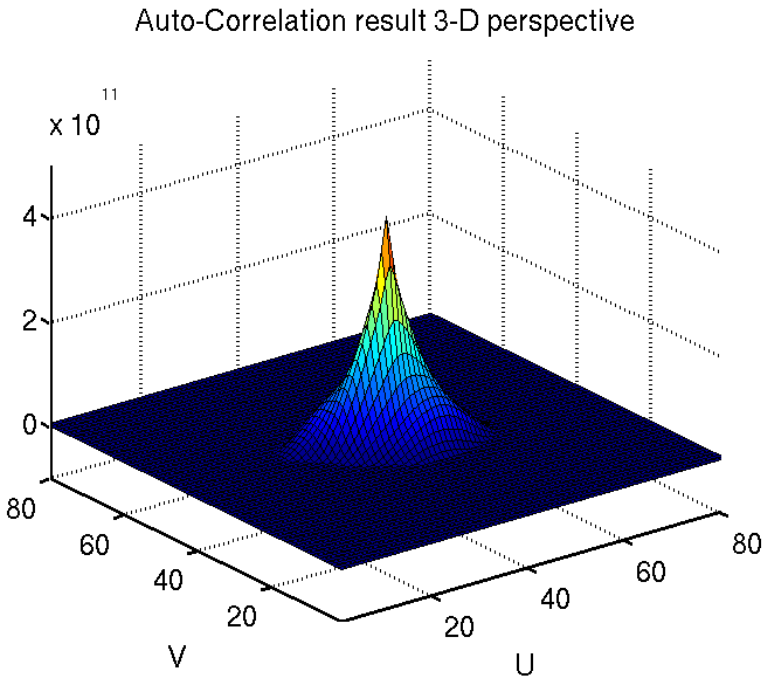

Figure 5.4 The auto-correlation result of figure 5.1 after isolating the correlation peak with an ellipse. The rest of $\mathcal{C}_{aa}$ has been set to 0, so that integrating outside of the fitted region will not effect ρ.

Chapter 6

Magnetic Memory: One-Dimensional Analysis

6.1 Effect of Field Cycling

In chapter 2 we explained how XRMS images were acquired at different field values along the magnetization loop. We analyzed magnetic memory based on the ascending and descending branches of the magnetization loop. Return Point Memory (RPM) and Conjugate Point Memory (CPM) are defined as follows: RPM tracks magnetic memory by acquiring an XRMS image at a given field value H and cross-correlating it with an image collected at the same field value H after cycling the entire loop (perhaps multiple times) (see Fig. 6.1). CPM tracks magnetic memory between the ascending and descending branches by cross-correlating images acquired at symmetrical field values (see Fig. 6.2).

We processed two sets of data (sets A and B) in order to analyze how RPM and CPM depend on field cycling. Data set A shows RPM and CPM behavior through five magnetization loops at field values of 0mT, 75mT and 150mT on the ascending

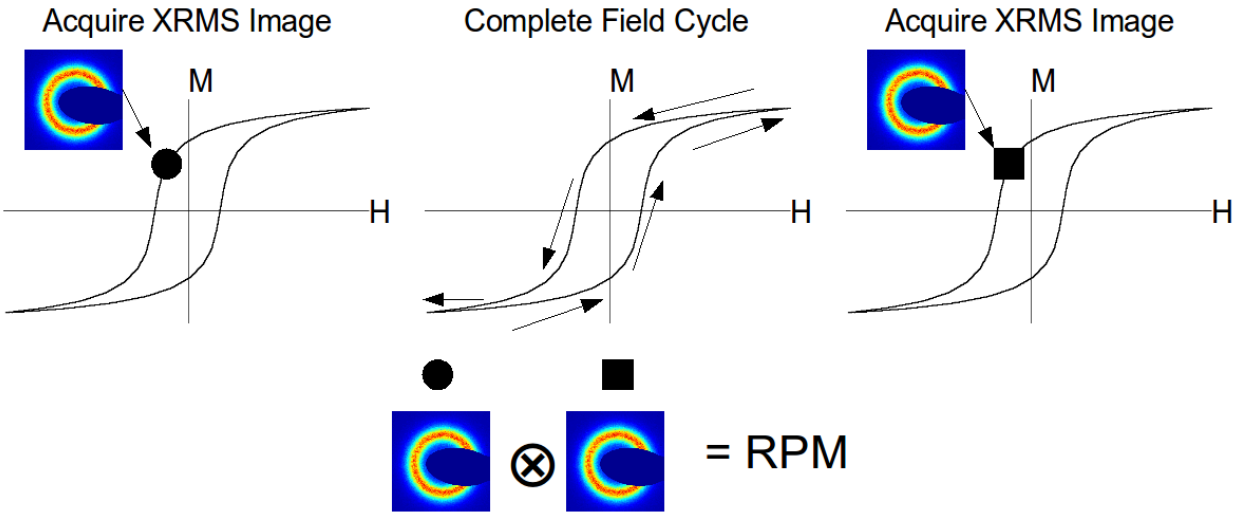

Figure 6.1 Return Point Memory

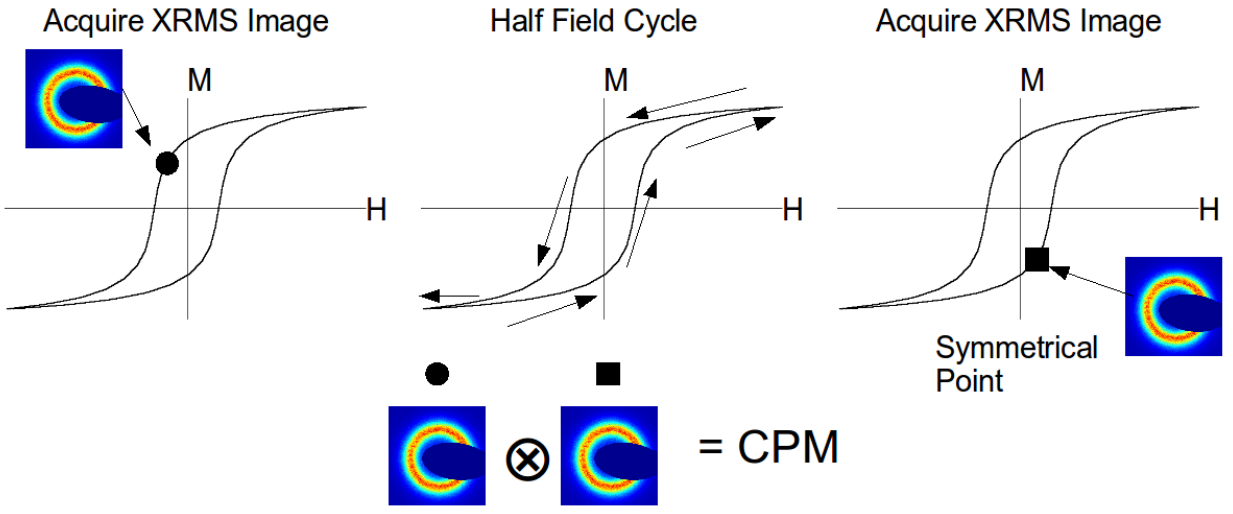

Figure 6.2 Conjugate Point Memory

branch, and at 0mT, -75mT and -150mT on the descending branch (see Fig. 6.3a). Data set B shows RPM and CPM behavior through seven magnetization loops and contains two additional field values: 37.5mT on the descending branch and -37.5mT on the ascending branch (see Fig. 6.3b). These additional field values allow for studying magnetic memory behavior at nucleation.

Sample preparation for sets A and B included a ZFC process (as described in chapter 2) down to about 20K. Because the sample was cooled in zero-field before acquiring XRMS images, sets A and B should not have possessed any macroscopic signs of exchange bias [2] between the ascending and descending branches.

As mentioned in section 5.1, degree of coherence (β) is a quantification of the amplitude of the speckle. For set B, $\beta = 13.9\%$ as opposed to set A where $\beta = 12.3\%$. This represents a 12.2% difference in β between the two sets, which is only a very slight difference. Therefore, magnetic memory behavior in either set does appear very similar (see Fig. 6.4).

6.1.1 Effect of Field Cycling for RPM

Graphs of RPM for set A are given in figures 6.4a and 6.4b. These graphs show that for fields near +75mT on the ascending branch and -75mT on the descending branch the sample exhibits strong RPM over 5 field cycles with ρ up to 95%. After 5 RPM field cycles, the sample exhibits only a slight 3.2% decrease in ρ at +75mT on the ascending branch. On the descending branch there is a decrease in ρ of only 1.4% at -75mT after 4 field cycles. Such strong magnetic memory characteristics indicate that when sample magnetization is near zero, the magnetic domain morphology reorders itself based on the exchange coupling between the [Co/Pd] FM multilayers and the IrMn AF layers [8]. Furthermore, this exchange coupling phenomenon is not strongly effected by the number of field cycles, and remains strong after many cycles.

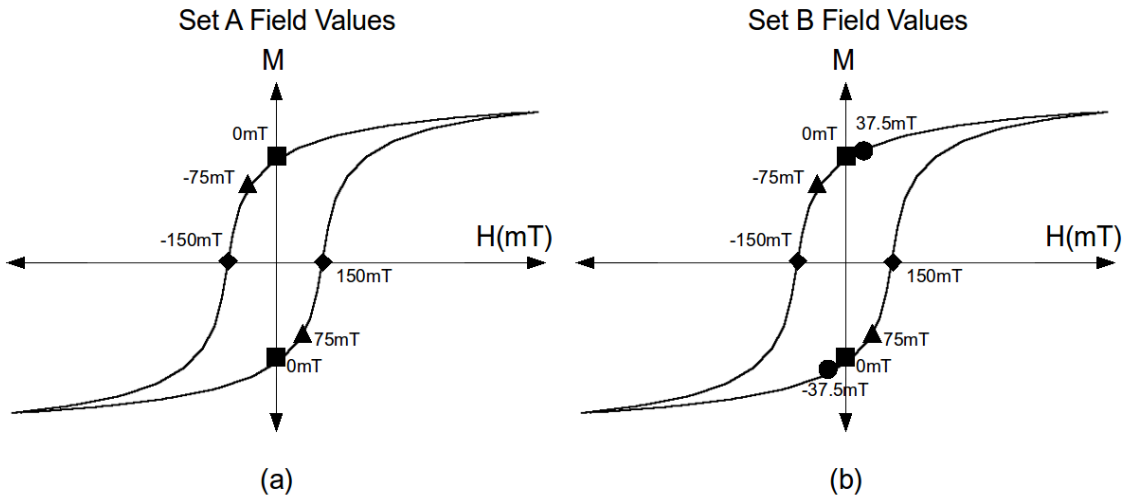

Figure 6.3 (a) Approximate locations on the hysteresis loop at which we acquired XRMS images for set A. Each point is coded by shape to match the corresponding graphs for RPM and CPM in figures 6.4a, 6.4b and 6.5a. (b) Approximate locations on the hysteresis loop at which we acquired XRMS images for set B. Each point is coded by shape to match the corresponding graphs for RPM and CPM in figures 6.4c, 6.4d and 6.5b.

For data set B RPM results are presented in figures 6.4c and 6.4d. At nucleation on the descending branch ($H = +37.5mT$) the sample exhibits low memory in the range of $\rho \sim 30\%$. However, at nucleation on the ascending branch ($H = -37.5mT$) the sample exhibits moderate memory with $\rho \sim 60\%$. We attribute this difference in memory between the two branches to be due to an unanticipated macroscopic exchange bias [18] that was not eliminated through the ZFC process.

Within the coercive region sets A and B show similar magnetic memory behavior. Both sets show strong RPM at +75mT and +150mT on the ascending branch and at -75mT and -150mT on the descending branch with $\rho > 80\%$. Also, within the coercive region magnetic memory is very stable through multiple field cycles. This result strengthens the position that when sample magnetization approaches zero, magnetic domain reconfiguration in the [Co/Pd] FM multilayers is driven by the frozen-in domain configuration in the IrMn AF layers [8].

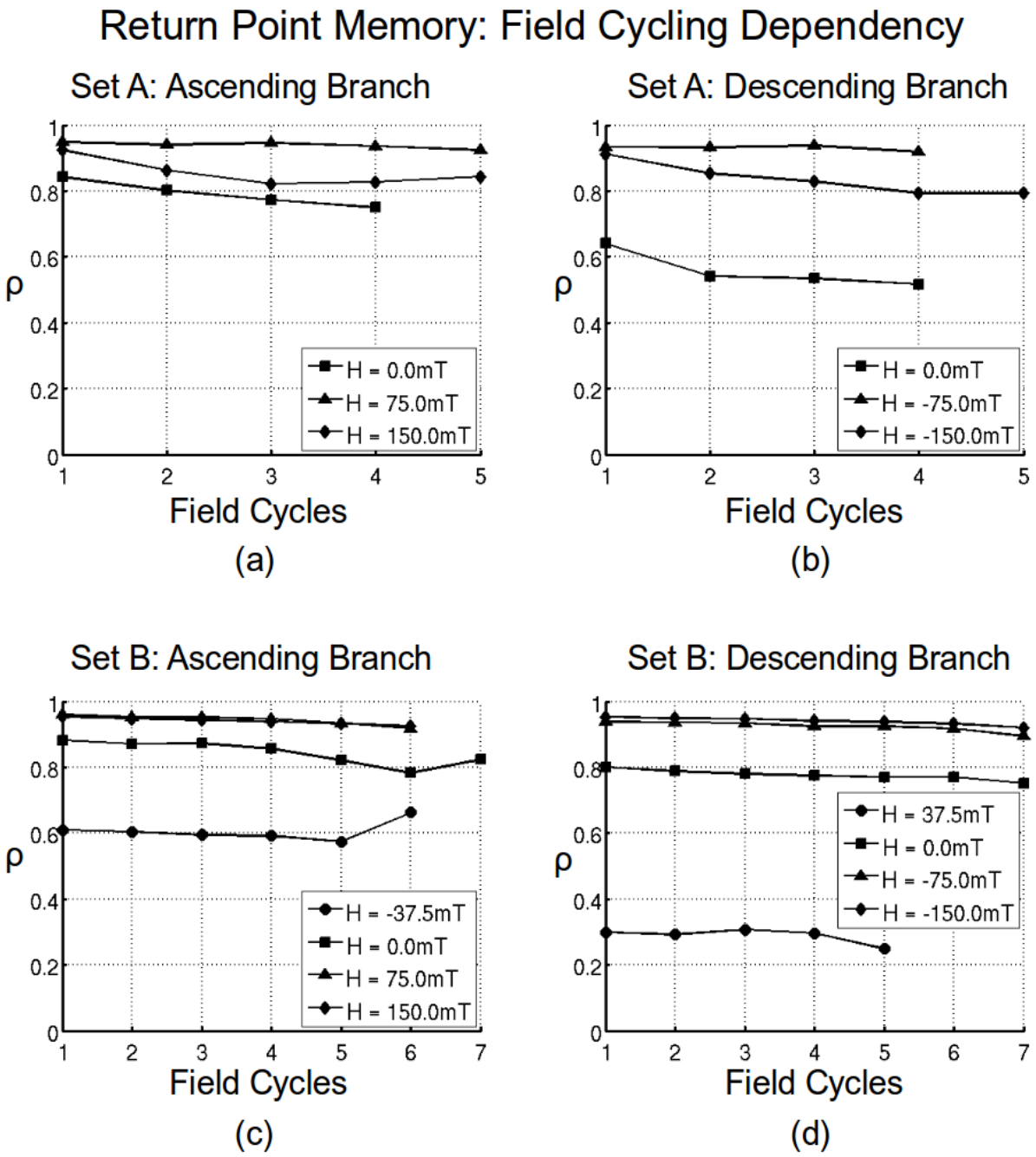

Figure 6.4 (a) $\rho \sim 0.95$ at a field of +75mT on the ascending branch. (b) At 0mT on the descending branch the decrease in ρ is 21.2% over 4 field cycles; whereas, on the ascending branch the decrease in ρ is only 11.7% over 4 field cycles. This difference is most likely due to a macroscopic exchange bias effect. (c) When H = -37.5mT on the ascending branch, an exchange bias phenomenon becomes clear. Comparing with (d), magnetic memory on the descending branch and the ascending branch is remarkably different.

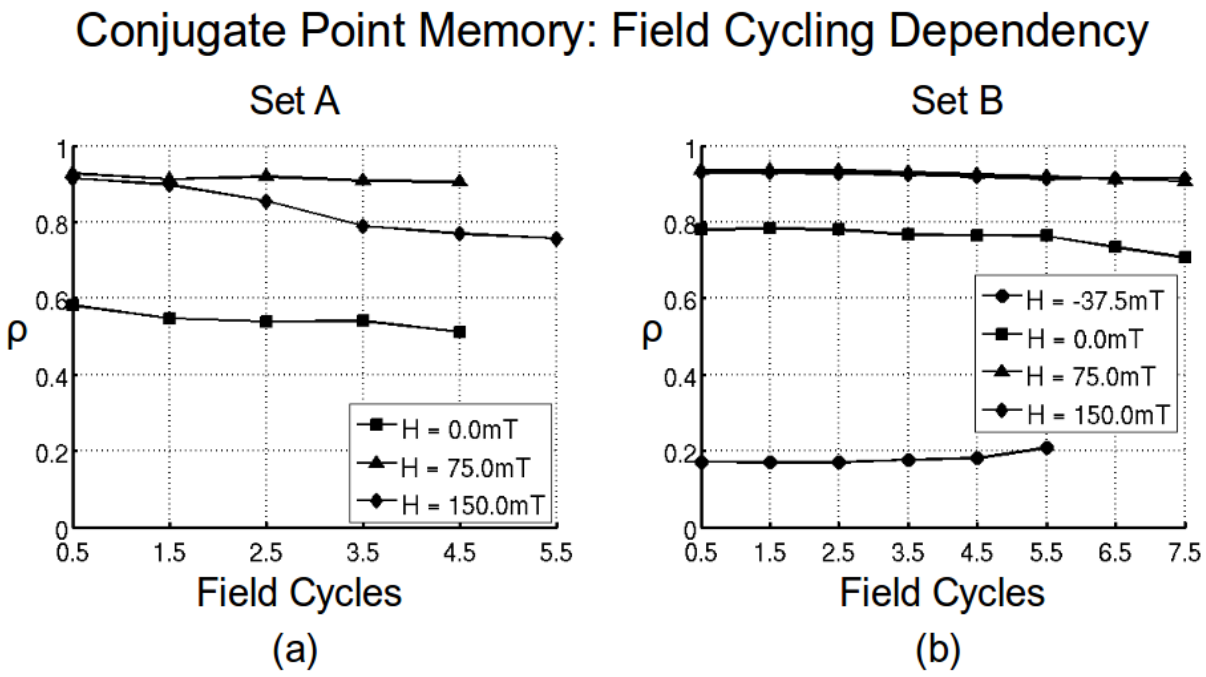

Figure 6.5 (a) CPM shows a marked decrease in ρ at H = 150mT. This decrease is also apparent in figures (6.4a) and (6.4b). However, this decrease in ρ does not occur in (b). This difference may be due to the lower β of set A compared with set B.

6.1.2 Effect of Field Cycling for CPM

The graph of CPM for data set A (see Fig. 6.5a) exhibits similar strong magnetic memory characteristics in comparison to the RPM graphs in figures 6.4a and 6.4b. At an external field of 75mT there is a decrease in ρ of only 2.4% over $4\frac{1}{2}$ field cycles. However, at 150mT the decrease in ρ is significantly more pronounce at 18% over $5\frac{1}{2}$ field cycles. Set B did not display the same decrease in ρ at 150mT.

Set B shows strong magnetic memory ($\rho > 90\%$) for half cycle separations at field strengths of 75mT and 150mT (see Fig. 6.5b). The relatively low memory at 37.5mT corresponds to the nucleation point on the hysteresis loop. When magnetic domains are just beginning to nucleate, it is somewhat less likely for similar magnetic domain configurations to occur between multiple field cycles [19].

6.2 Magnetic Memory Dependency with Field Value

We measured ρ over a range of H values in order to plot $\rho(H)$. Each $\rho(H)$ value in a graph of field dependence is the average of all RPM or CPM ρ values for a given H (averaging all cycles). If n field cycling dependent data points exist at field H, then the average of these data points produces a single $\rho(H)$ value. Plotting $\rho(H)$ produces graphs that describe the field dependent RPM and CPM behavior of the sample.

We analyzed five sets of data to quantify field dependence of magnetic memory. Sets A and B are the same sets analyzed for field cycling dependence. These sets are not optimized for studying the full hysteresis loop of the sample, because they do not contain a sufficient range of H values. However, they do indicate a tendency for stronger magnetic memory at field strengths above 75mT.

In order to collect the third set of data, set C, we subjected the sample to a complete demagnetization cycle and zero-field cooled it down to 18K before acquiring XRMS images. Because we began gathering data after a complete demagnetization cycle (no remanent field), as mention in section 2.5 it is necessary to separate the first magnetization branch from the rest of the major cycle/loop (see Fig. 2.8). However, because we cycled the field only twice when collecting this set, RPM plots for the ascending branch and descending branch do not appear symmetrical. This is because in order to plot a graph for the descending branch, we needed to use the first magnetization cycle data. Therefore, while the graph for the descending branch is not strictly a true RPM graph, it still has a shape that is consistent with predicted RPM behavior.

The degree of coherence in set C is $\beta = 9.3\%$. This degree of coherence is about 40% lower than in set B. This indicates that the amplitude of coherent signal data in

this set is somewhat reduced compared with sets A and B. This reduction in speckle amplitude made it slightly more difficult to use (4.7) in order to isolate coherent signal data. Therefore, the RPM and CPM graphs of $\rho(H)$ may not be as accurate as those given for sets A and B.

For set D, $\beta = 8.9\%$, which is approximately the same amount of speckle amplitude as in set C. Similarly to set C we began gathering data after a complete demagnetization cycle. Therefore, it is necesseary to separate the first magnetization branch from the major branch when plotting $\rho(H)$ for set D.

Each data point in the RPM graph of $\rho(H)$ for set D corresponds to the average of up to six separate cross-correlations. This is opposed to the single cross-correlation per data point in the RPM graph of $\rho(H)$ for set C. Thus, the shape of set D's RPM graph is smoother and more symmetrical between the ascending and descending branches.

Set E consists of 8 full magnetization cycles including the first magnetization branch. We have left out the first magnetization branch in generating the RPM and CPM graphs of $\rho(H)$. In this set $\beta = 8.5\%$, which again is similar to sets C and D, but is also the lowest degree of coherence for all of our data sets. The lower β made it more difficult to distinguish coherent from incoherent signal during pre-separation, and may reduce some confidence in the accuracy of magnetic memory results.

6.2.1 Field Dependence of RPM

The RPM field dependence graph for set A (see Fig. 6.6a) shows very high magnetic memory ($\rho > 90\%$) at a field strength of +75mT on the ascending branch and at -75mT on the descending branch. Memory then decreases slightly at +150mT on the ascending branch ($\rho \sim 84\%$) and -150mT on the descending branch ($\rho \sim 82\%$). However, set B does not show this same decrease in magnetic memory at 150mT (see Fig. 6.6a). Indeed, magnetic memory appears to increase at field values above 75mT.

For set C, we acquired images at 37.5mT intervals from -450mT to +450mT. We cycled the field twice for this set beginning with the descending branch. This set yields information about the magnetic memory behavior of the sample over a much wider range of fields compared to sets A and B (see Fig. 6.6b). This set indicates low memory at nucleation, higher memory in the coercive region and then a return to low memory at saturation. Because each data point consists of a single cross-correlation, the graph is not as smooth as the RPM graph for set D (see Fig. 6.6c).

The RPM field dependence graph for set D shows $\rho(H)$ with shorter step size near nucleation. Near nucleation the sample exhibits a steady increase in magnetic memory ($\rho \sim 20\%$ to $\rho \sim 60\%$) on the ascending and descending branches. Maximum magnetic memory ($\rho \sim 90\%$) is achieved in the coercive region where $H = +112.5mT$ on the ascending branch and $H = -112.5mT$ on the descending branch. When the magnetic domains begin to saturate, there is a decrease in signal strength, which leads to a gradual decrease in magnetic memory on either branch eventually falling to $\rho \sim 15\%$.

Set E contains even more data points near nucleation than set D, and contains higher resolution field information at saturation (see Fig. 6.6d). We acquired data between field values of -75mT and 150mT on the ascending branch at intervals of 15mT. On the descending branch we acquired data at the same intervals between field values of 75mT and -150mT. This high resolution data covers nucleation and part of the coercive region. At saturation we acquired data for field values of 375mT to 525mT at 15mT intervals on the ascending branch, and from -375mT to -525mT at 15mT intervals on the descending branch. Like sets C and D, this set also shows that the exchange coupling effect has the greatest influence on magnetic memory within the coercive region [8].

6.2.2 Field Dependence of CPM

CPM results between sets A and B (see Fig. 6.7a) show excellent agreement of magnetic memory at $H = 75mT$ where both sets yield $\rho \sim 92\%$. Set A still produces a downward trend in magnetic memory at 150mT dropping by 11.5% compared with ρ(75mT). This drop in magnetic memory does not occur for set B. Set B shows low memory ($\rho \sim 20\%$) at nucleation. This indicates a smaller likelihood for magnetic domains to retain similar configurations over multiple field cycles when domains are just beginning to nucleate [19].

The CPM graph for set C (see Fig. 6.7b) posseses a similar shape to either branch of its RPM graph in figure 6.6b. The smoother shape of the CPM graph is due to more averaging at each data point. The CPM graph shows low memory at nucleation ($\rho \sim 30\%$), higher memory in the coercive region ($\rho \sim 80\%$) and a return to low memory at saturation ($\rho \sim 25\%$) similar to the RPM graph.

Sets D and E show expected CPM behavior (see Fig. 6.7c and Fig. 6.7d). The shape of the CPM graph for either set shows low memory at nucleation ($\rho \sim 15\%$ for set D), higher memory in the coercive region ($\rho \sim 87\%$ for set D) and back to lower memory at saturation ($\rho \sim 15\%$ for set D).

6.3 One-Dimensional Analysis Conclusions

This one-dimensional magnetic memory analysis indicates that the magnetic domain configuration in the [Co/Pd] FM multilayers aligns with the frozen-in domain configuration in the AF layers when net sample magnetization approaches zero (coercive point) [8]. This phenomenon is observed in the ZFC state at low temperatures (below the IrMn blocking temperature), but is not observed above the blocking temperature. Specifically, at room temperature this sample exhibits no magnetic memory proper-

ties. Although for this sample T_B is very close to room temperature, ensuring that temperatures remain below the blocking temperature is vital to our sample's magnetic memory characteristics.

Magnetic memory is highest within the coercive region, and even exhibits a plateau that usually coincides within a field range of $75mT < H < 300mT$. This behavior is produced by every data set we have analyzed. Additionally, when sample magnetization is close to nucleation or saturation, magnetic memory is lower. Indeed, at nucleation or saturation exchange coupling is less effective at driving domain alignment, because there is more overall randomness in distribution of domains that may be coerced into aligning with the underlying AF domain pattern. Therefore, it is less likely for similar domain configurations to occur over multiple field cycles at nucleation or saturation.

These findings indicate that the exchange coupling phenomenon is a useful means of imparting magnetic memory properties to our sample. Additional analysis to show how magnetic domain morphology varies within the coercive region, at nucleation and at saturation in the form of two-dimensional magnetic memory maps is presented in the following chapter. These maps will assist in understanding how the individual magnetic domains are being altered by the applied magnetic field (in one direction or the other), and how that alteration is still highly dependent on the underlying AF domain pattern.

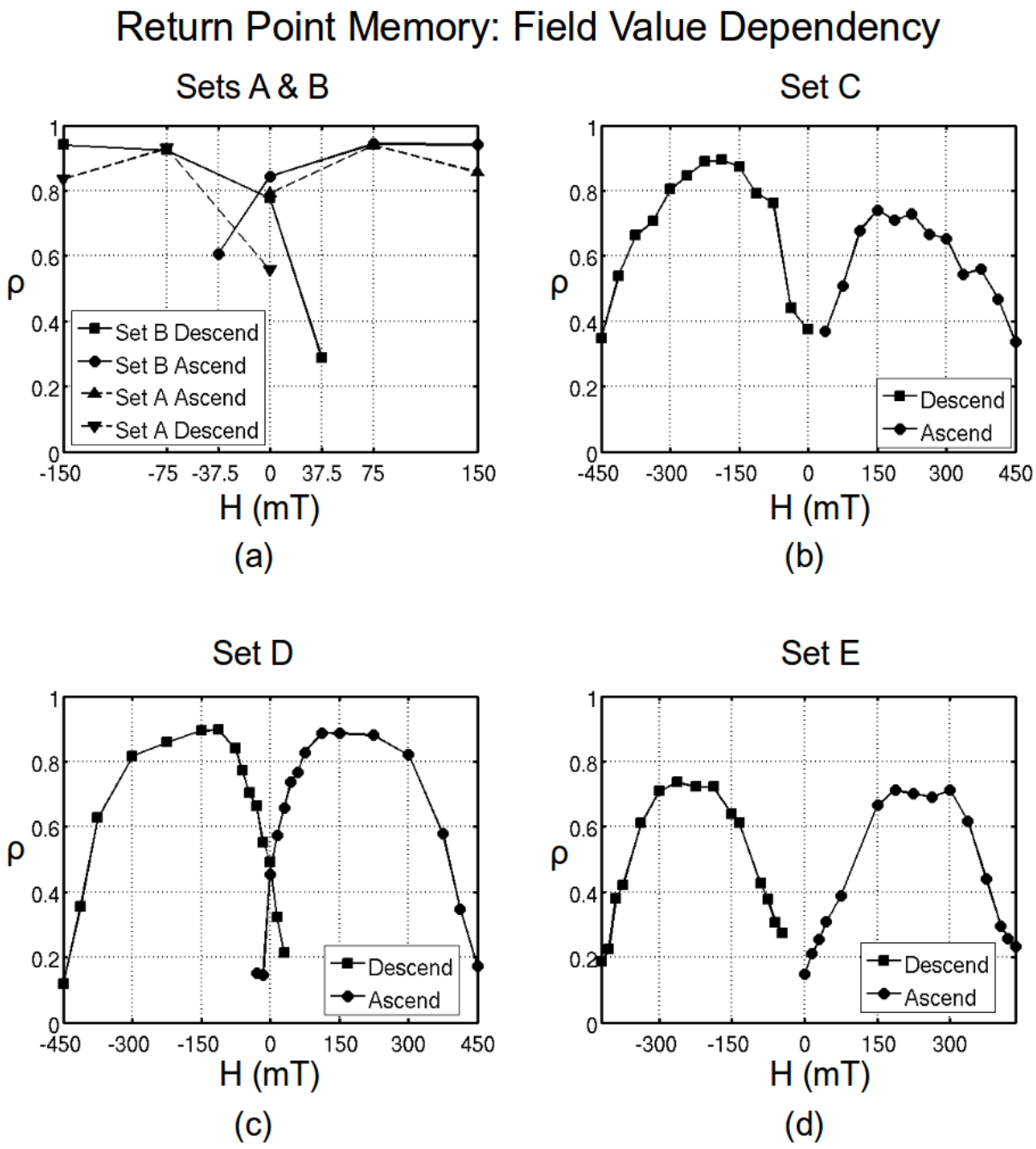

Figure 6.6 (a) Sets A and B show very similar magnetic memory behavior. At $H = 75mT$ they align very closely. (b) The descending branch contains the first magnetization loop, which causes asymmetry in RPM between the two branches. (c) The descending branch and ascending branch display excellent symmetery. Maximum ρ is achieved at $H = 112.5mT$ where $\rho \sim 90\%$. (d) Also displays excellent symmetry after deleting some data points with erratic memory behavior.

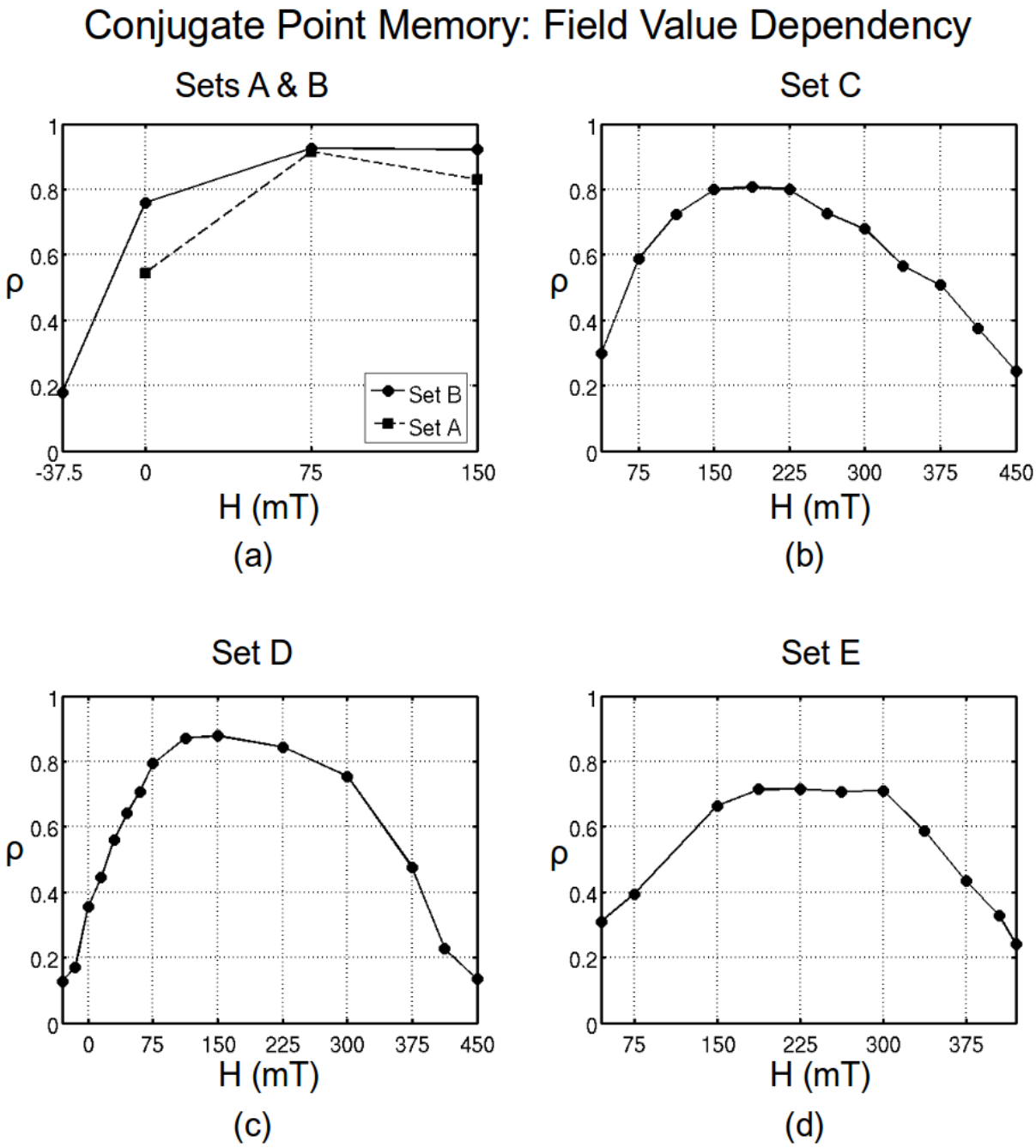

Figure 6.7 (a) Nucleation ($H = -37.5mT$) indicates lower CPM. Sets A and B show similar CPM behavior. (b) In the coercive region CPM is strong with $\rho \sim 80\%$. Graphs (b), (c) and (d) all show very similar CPM behavior with low memory at nucleation, higher memory within the coercive region and a return to low memory at saturation. (c) Maximum CPM is achieved at $H = 150mT$ just as in sets B and C. (d) Maximum CPM is achieved at $H = 187.5mT$.

Chapter 7

Magnetic Memory: Two-Dimensional Analysis

7.1 Memory Maps

Two-dimensional maps of magnetic memory give a larger view of the magnetic memory behavior of our sample. Constructing memory maps requires cross-correlation between all possible pairs of XRMS images in a data set. If image a was acquired at field H_1 and if image b was acquired at field H_2 then ρ for $\mathcal{C}_{ab}$ is placed on the memory map at coordinates (H_1, H_2), where $0 \leq \rho(H_1, H_2) \leq 1$.

Generating magnetic memory maps requires many more cross-correlations than for the one-dimensional case. For example, set D contains 121 XRMS images. Generating the corresponding memory maps for set D requires $121^2 = 14641$ cross correlations. Efficiency is vital. This is the reason for taking advantage of operation (3.2) the fastest cross-correlation algorithm available.

We generated memory maps for all of the data sets except set A. Set A did not allow for two-dimensional memory maps, due to the ordering in which we acquired

data. Memory maps for data set D are able to show detailed two-dimensional memory behavior at nucleation, the coercive region and saturation, so a two-dimensional memory analysis of set D will be the primary focus of this chapter.

7.2 Memory Map Construction Details

Each $\rho(H_1, H_2)$ in a memory map is the average of all possible $\rho(H_1, H_2)$ values for the same number of field cycle separations. If image a was acquired during field cycle n and image b was acquired during field cycle m then (for RPM) the number of cycle separations is $s = |n - m|$. Therefore, $s = 0, 1, 2, ...$, so each RPM map corresponds to a different number of full-cycle separations. If image a was acquired during field cycle n, and if image b was acquired on the opposite branch of the hysteresis loop during field cycle m then the separation for CPM is given by operation (7.1).

$$s = \begin{cases} |n - m - \frac{1}{2}| & n \geq m \\ m - n + \frac{1}{2} & n < m. \end{cases} \tag{7.1}$$

Therefore, $s = 0.5, 1.5, 2.5, ...$, so each CPM map corresponds to a different number of half-cycle separations.

The ρ value associated with $\mathcal{C}_{ab}$ (the correlation pattern with a and b separated by s field cycles) is placed on the s^{th} map (M_s). M_s contains the average of all possible $\rho(H_1, H_2)$ separated by s field cycles. If s_0 corresponds to the smallest possible RPM or CPM separation, then M_{s_0} usually has higher $\rho(H_1, H_2)$ than $M_{s_1}, M_{s_2}, M_{s_3}, ...$

For RPM maps there is a specific case of $n = m$, i.e. $s = 0$. For this case the diagonal where $H_1 = H_2$ corresponds to auto-correlating each image with itself; thus, resulting in $\rho = \frac{\sum \mathcal{C}_{aa}}{\sqrt{\sum \mathcal{C}_{aa} \sum \mathcal{C}_{aa}}} = 1$ (see Fig. 7.1).

When we present maps of magnetic memory, we do so in a quadrant format: RPM maps are given for the ascending branches cross-correlated with the ascend-

ing branches or for the descending branches cross-correlated with the descending branches. These RPM maps are located in the figures' upper right and lower left quadrants respectively (see Fig. 7.1). We also present CPM maps, which either cross-correlate ascending branches with descending branches or the opposite order. Order of operations makes no difference in calculating ρ, so the two CPM maps are identical, but both are included for completeness of the quadrant layout. The CPM maps are located in the upper left and lower right quadrants. In addition, each map figure indicates how many cycle separations the maps correspond to. It is interesting to compare maps of RPM and CPM as s varies. A comparison shows that magnetic memory is quite stable regardless of field cycles when H corresponds to the coercive region.

7.3 Two-Dimensional Field Dependence of RPM and CPM

The maps for Set D show magnetic memory behavior at nucleation, within the coercive region and at saturation. Figures 7.1a and 7.1d show CPM results for $s = 0.5$, and figures 7.1b and 7.1c show RPM results for $s = 0$. The RPM maps show $\rho = 1$ along the diagonal where $H_1 = H_2$ (auto-correlations). Both RPM and CPM maps indicate strong magnetic memory within the coercive region where $(75mT, 75mT) \leq (H_1, H_2) \leq (350mT, 350mT)$. Within this region $\rho \geq 70\%$.

Figure 7.2 shows magnetic memory for $s = 1$ for RPM ((b) and (c)) and for $s = 1.5$ for CPM ((a) and (d)). After one field cycle, it is possible to observe slightly stronger RPM on the descending branch than on the ascending branch. RPM on the descending branch reaches a maximum value of $\rho_{max} \sim 93.5\%$; whereas, maximum RPM on the ascending branch reaches a value of $\rho_{max} \sim 90.2\%$. This slight magnetic

memory preference is possibly due to a macroscopic exchange bias [18]. Even though the ZFC procedure should remove this exchange bias, it may be the case that this sample still presents some natural bias that was not eliminated through the ZFC process.

An exchange bias also appears to exist after 2 field cycles in Figure 7.3. This figure shows RPM for $s = 2$ and CPM for $s = 2.5$. RPM on the descending branch achieves a maximum value of $\rho_{max} \sim 91\%$; whereas, RPM on the ascending branch reaches a slightly lower maximum value of $\rho_{max} \sim 88.5\%$. Also, there is still a large memory plateau centered on the coercive region that is very similar to the plateau visible for $s = 1$. The proportions of the plateau are still the same and maximum magnetic memory is still very close showing a decrease in ρ_{max} of only 2.7%.

After 3 field cycles, we did not have sufficient data to produce an RPM map for the ascending branch. However, Figure 7.4 shows RPM for $s = 3$ on the descending branch and CPM for $s = 3.5$. Magnetic memory within the coercive region plateau stays above 65% for RPM and CPM. Maximum RPM is still very high with $\rho_{max} \sim$ 90% on the descending branch. This represents only a 3.8% decrease in magnetic memory compared with the descending branch for $s = 1$. These results indicate that magnetic memory is strongly independent of field cycling when the external field matches the coercive region of the sample [8].

Set E contains high resolution field information that allows for the creation of magnetic memory maps that show high levels of detail at nucleation, part of the coercive region and saturation. The memory maps for $s = 1$ for RPM and for $s = 1.5$ for CPM are given in figure 7.5. Regardless of this set's lower β, the magnetic memory behavior still indicates low ρ at nucleation, a magnetic memory plateau within the coercive region with higher ρ of roughly the same dimensions as that seen in set D and a return to low memory at saturation. The fact that two separate sets of data

indicate the same general two-dimensional magnetic memory morphology is evidence that exchange coupling is a useful means for controling magnetic memory behavior within the coercive region [8].

7.4 Two-Dimensional Analysis Conclusions

As it was previously mentioned in chapter 6, the reason for higher memory within the coercive region is due to an exchange coupling effect between the (IrMn) AF layers and the [Co/Pd] FM multilayers [8]. When net magnetization in the sample approaches zero, it is more energetically favorable for the magnetic domains in the FM multilayer to match the underlying domains in the AF layer (see Fig. 2.3) [4]. The frozen-in domain pattern present in the AF layers plays the role of a template for the domain configuration in the FM multilayers. Therefore, higher memory in the coercive region follows as a natural consequence of this coupling effect [8].

RPM and CPM maps show a large central plateau with high value of ρ that occupies an area around the coercive point. This memory plateau is very stable: even after multiple field cycles the decrease in ρ is only a few percent. This indicates that the magnetic domain pattern in the FM multilayer is strongly determined by the AF underlying template. Also, a slight deviation in applied field ΔH has very little effect on the domain pattern. Locally, the domain walls may move somewhat, but the overall shape and configuration of the domains remains largely governed by the underlying AF template. This is the reason for the existance of the coercive region plateau in the RPM and CPM maps.

Memory maps also show excellent symmetry between $\rho(H_1, H_2)$ versus $\rho(H_2, H_1)$. This is a consequence of the ZFC process and indicates that macroscopic exchange bias is largely non-existant, and the descending and ascending branches of the mag-

netization cycle are very symmetrical. Had the sample been cooled in the presence of an external field then the location of the coercive region plateau would be offset, and there would be less symmetry on either side of the diagonal where $H_1 = H_2$. This opens perspectives of further analysis in field cooled states, to study how the exchange bias may effect the shape, size and magnitude of the magnetic memory plateau in this system.

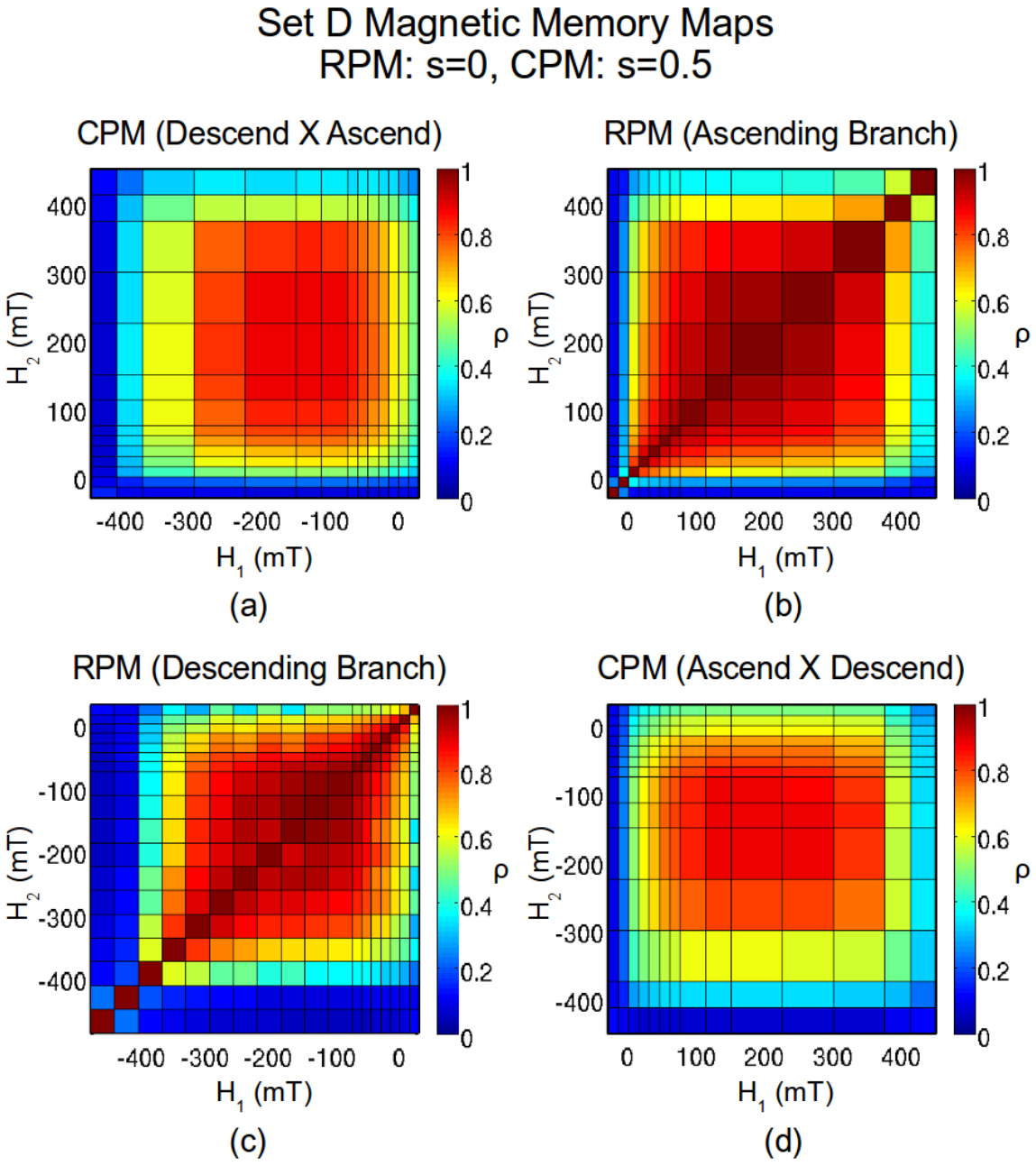

Figure 7.1 RPM ($s = 0$) and CPM ($s = 0.5$) maps. (a) and (d) show CPM while (b) and (c) show RPM. RPM maps show ones along the diagonal where $H_1 = H_2$ (auto-correlations). RPM and CPM maps show a memory plateau centered within the coercive region where $\rho \geq 70\%$. The memory plateau occupies the region where approximately $(75mT, 75mT) \leq (H_1, H_2) \leq (350mT, 350mT)$.

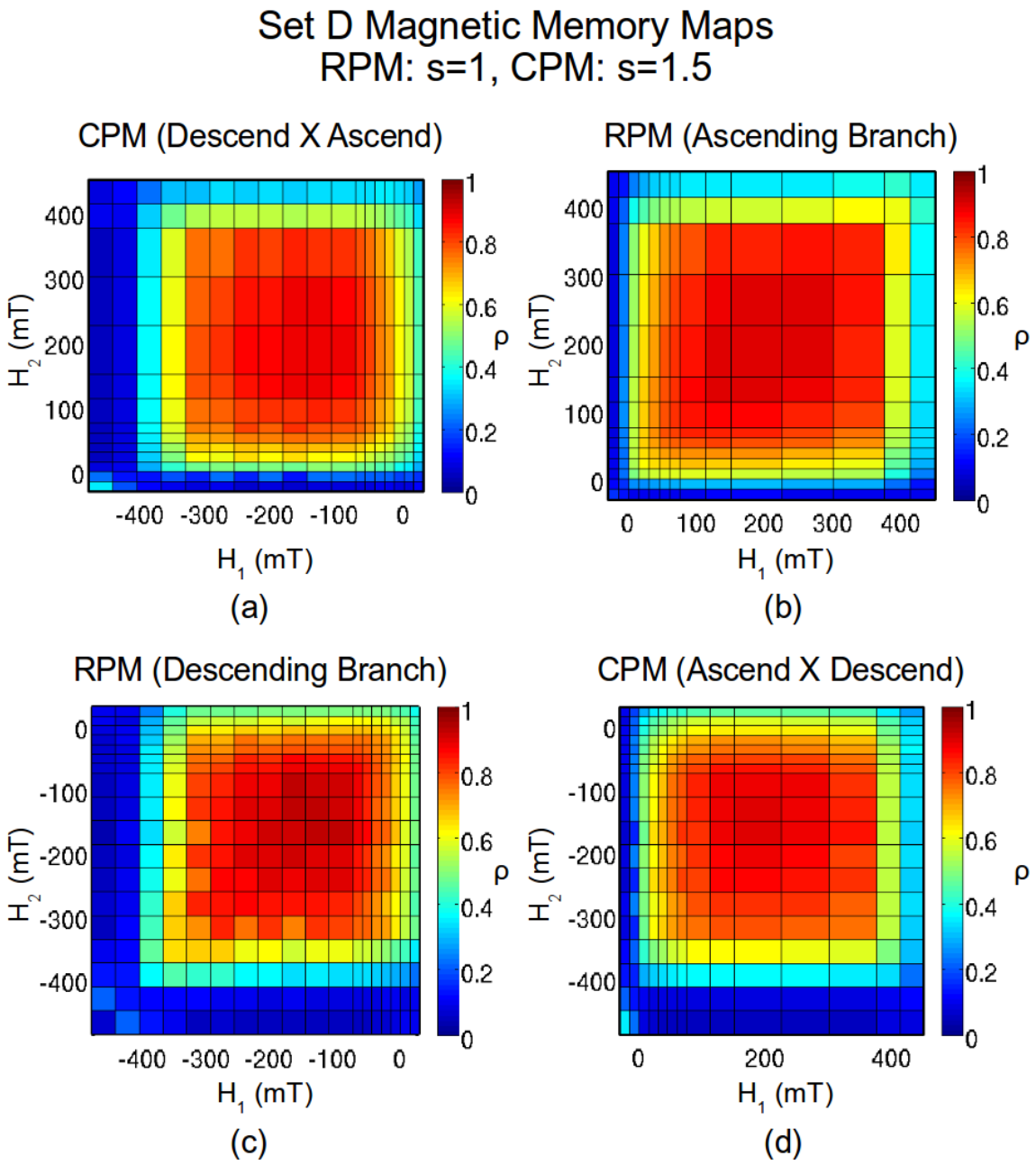

Figure 7.2 RPM ($s = 1$) and CPM ($s = 1.5$) maps. The memory plateau has a slightly stronger maximum in (c) as opposed to (b) ($\rho_{max} \sim 93.5\%$ as opposed to $\rho_{max} \sim 90.2\%$). This preference for stronger RPM on the descending branch as opposed to the ascending branch is probably due to a macroscopic exchange bias that was not eliminated through the ZFC process. Maximum magnetic memory within the coercive region plateau for CPM is around $\rho_{max} \sim 89\%$.

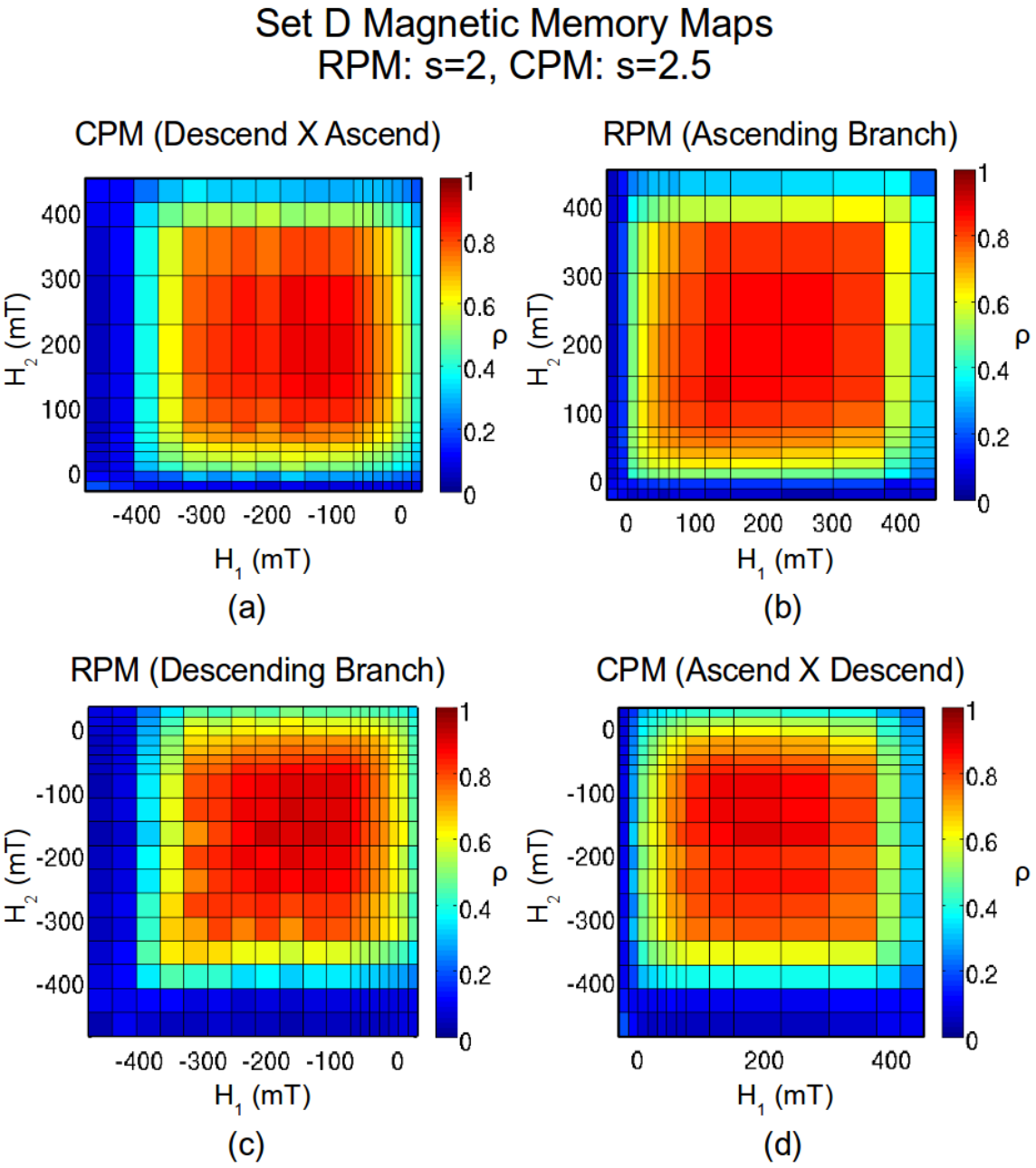

Figure 7.3 RPM ($s = 2$) and CPM ($s = 2.5$) maps. After 2 field cycles, the memory plateau persists with $\rho_{max} \sim 88.5\%$ in (b) and $\rho_{max} \sim 91\%$ in (c). There is still a tendency for slightly higher ρ on the descending branch. (a) and (d) also continue to show the coercive region memory plateau with $\rho_{max} \sim 89\%$ as in figure (7.2). Field cycling has only a small effect on magnetic memory within the coercive region.

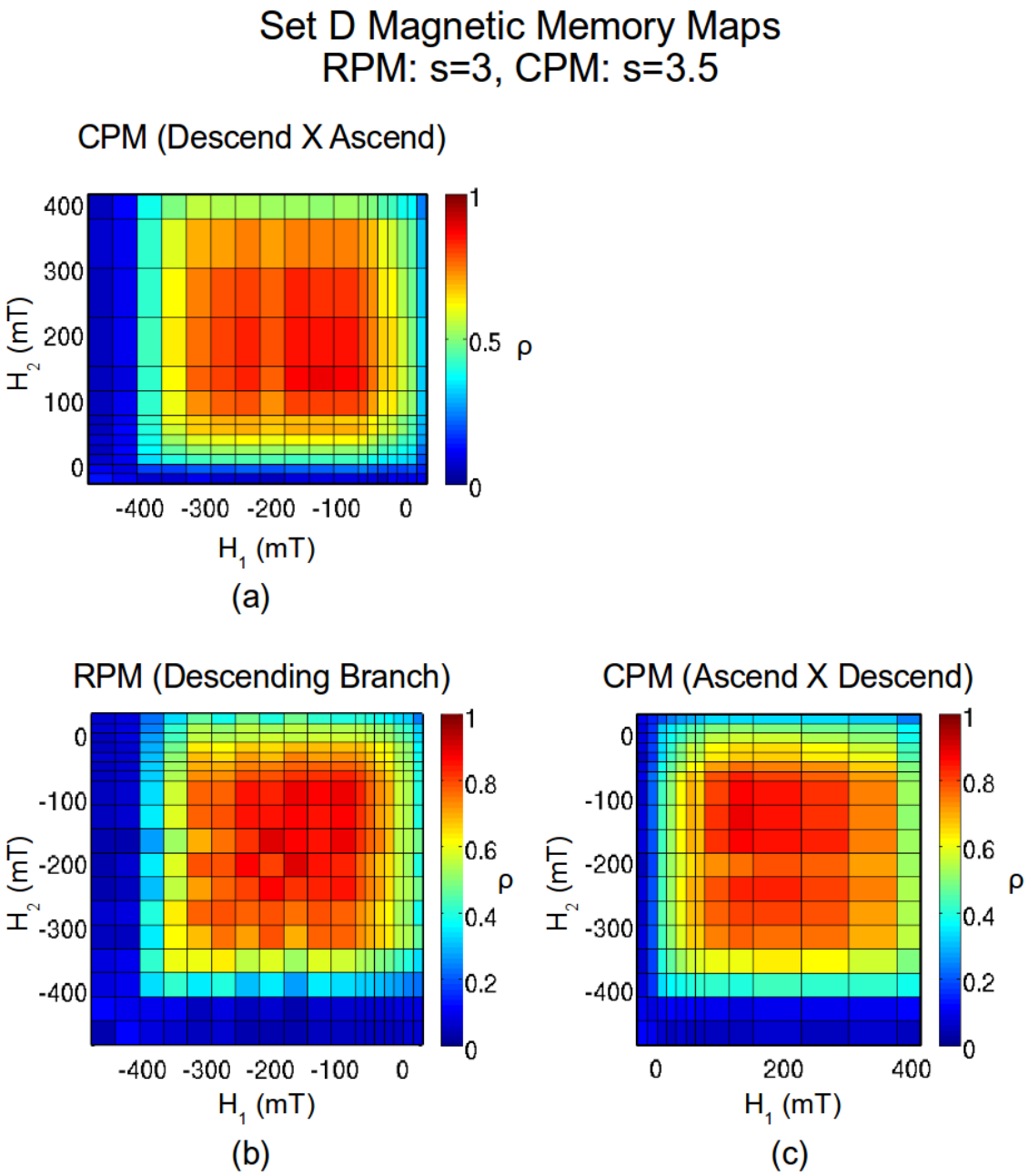

Figure 7.4 RPM ($s = 3$) and CPM ($s = 3.5$) maps. There is not sufficient data to create a memory map for the ascending branch after 3 field cycles. However, all remaining RPM and CPM maps still exhibit the coercive region memory plateau where $\rho \geq 65\%$ for $(75mT, 75mT) \leq (H_1, H_2) \leq (350mT, 350mT)$. Also, field cycling has had only a modest effect on the memory plateau. In figure (7.2c) $\rho_{max} \sim 93.5\%$; whereas, in (c) in this figure $\rho_{max} \sim 90\%$, which represents only a 3.8% decrease in magnetic memory.

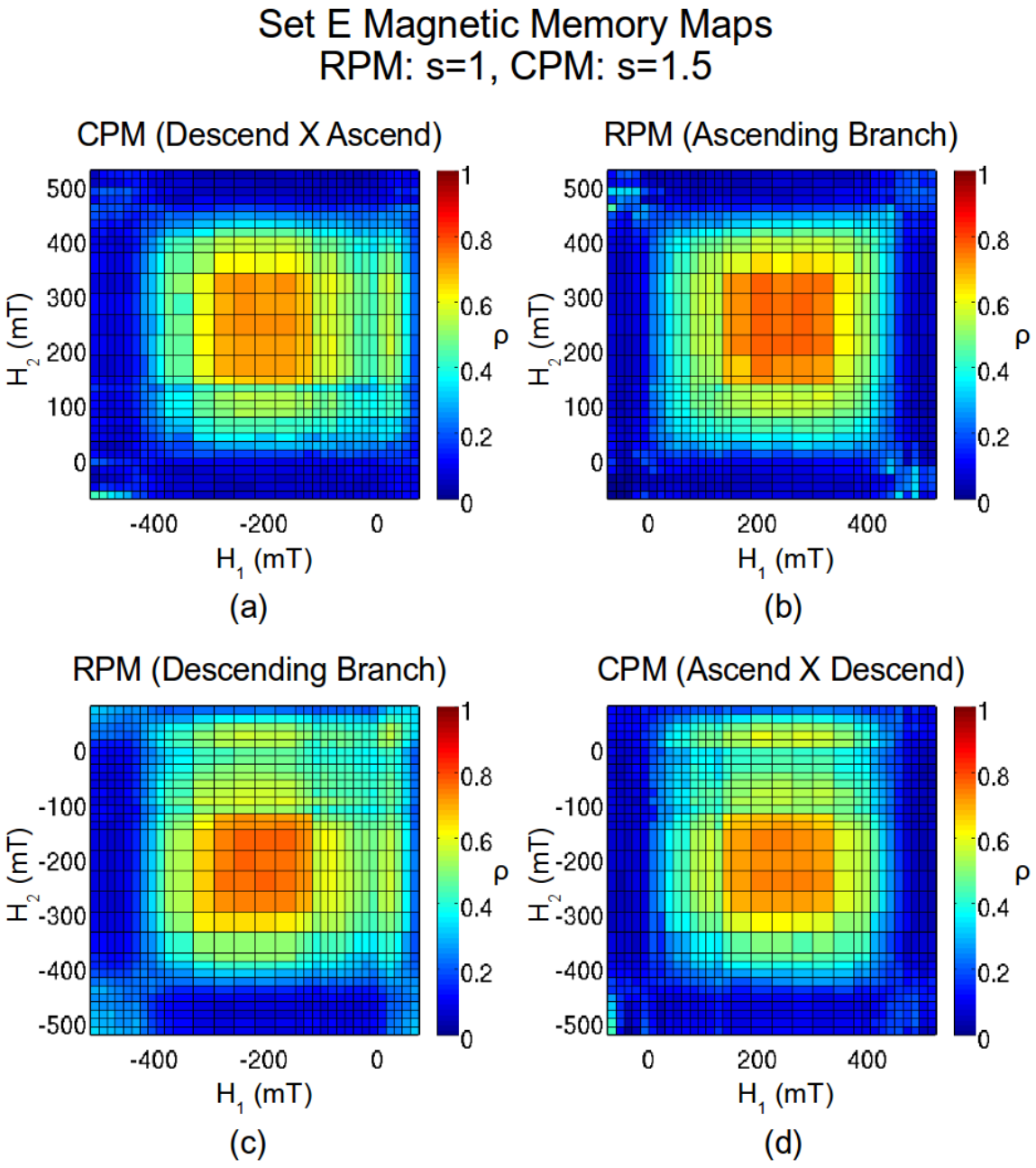

Figure 7.5 RPM ($s = 1$) and CPM ($s = 1.5$) maps for set E. The magnetic memory plateau is visible for set E. The proportions of the plateau are similar compared with the memory maps for set D. This map displays higher resolution field information at nucleation and saturation than set D. Although ρ_{max} is lower than in set D, the morphology of the magnetic memory behavior is similar with lower memory at nucleation and saturation, and higher memory within the coercive region.

Chapter 8

Summary & Conclusion

We have studied a $([Co(4Å)/Pd(7Å)]_{12}IrMn(24Å))_4$ FM/AF multilayer thin film by placing it within a variable magnetic field while illuminating it with coherent soft x-rays in transmission geometry. By this means we have detected XRMS patterns that relate to the local magnetic domain morphology in the sample.

XRMS patterns are highly dependent on H, because H alters the magnetization, and hence, the domain configuration of the sample. We cross-correlated XRMS patterns detected under varying H in order to determine the degree of similarity between magnetic domain configurations under different external field conditions. We did this as a means of understanding the sample's magnetic memory characteristics. However, before cross-correlation was possible, it was necessary to separate coherent and incoherent scattering signal present in the XRMS patterns.

Isolation of pure coherent scattering signal is most effectively achieved through XRMS image averaging. We attempted coherent signal isolation through 2D least-squares fitting of whole XRMS images, but this technique caused either oscillation artifacts or dicontinuities, which corrupted the isolated signal (cross-correlation of corrupted coherent signal led to unexpected memory results).

Image averaging is the best method for coherent/incoherent signal separation. We tried several different algorithms to accomplish image averaging. An FFT based image averaging algorithm is the best, due to its high speed. The purpose of image averaging is to approximate incoherent signal, which would have been experimentally obtained had the incident x-ray light not been coherent. Our image processing program uses the approximated incoherent signal in order to extract pure coherent scattering signal from the XRMS images.

Cross-correlation of coherent scattering signal is most efficiently accomplished by means of an FFT based algorithm. FFT based cross-correlation is so much faster than the purely iterative alternative that on a standard quad-core based desktop computer we were able to produce the hundreds of thousands of cross-correlations necessary to generate magnetic memory results in only a few hours.

It is necessary to integrate cross-correlation results in order to calculate ρ. Only a small region of the cross-correlation pattern is useful for determining ρ (typically the size of the average speckle spot). We developed an algorithm to fit an ellipse around the useful signal within a cross-correlation result.

We analyzed the effect of field cycling and field strength dependence of magnetic memory. The sample exhibits strong one-dimensional and two-dimensional RPM and CPM within the coercive region. The coercive region corresponds to field strengths from about 75mT to about 300mT. Outside of the coercive region the sample exhibits low memory at nucleation and at saturation. The exchange coupling effect between the IrMn AF layers and the [Co/Pd] FM multilayers are the origin of magnetic memory properties: when the net magnetization in the FM multilayers approaches zero (coercive point), the FM domain pattern matches the AF frozen domain pattern. Furthermore, the 2D analysis of magnetic memory indicates that high memory charcteristics are very stable against field deviations from the coercive point. In conclusion,

we have shown that AF coupling can induce very strong magnetic memory in FM layers, and the magnetic memory is very stable with field deviations from the coercive point.

Bibliography

[1] Gary A. Prinz. Magnetoelectronics. *Science*, 282(5394):1660–1663, 1998.

[2] J. Nogus and Ivan K. Schuller. Exchange bias. *Journal of Magnetism and Magnetic Materials*, 192(2):203 – 232, 1999.

[3] Charles Kittel. Theory of the structure of ferromagnetic domains in films and small particles. *Phys. Rev.*, 70(11-12):965–971, Dec 1946.

[4] S. Maat, K. Takano, S. S. P. Parkin, and Eric E. Fullerton. Perpendicular exchange bias of *co/pt* multilayers. *Phys. Rev. Lett.*, 87(8):087202, Aug 2001.

[5] K. Chesnel, M. Belakhovsky, F. Livet, S. P. Collins, G. van der Laan, S. S. Dhesi, J. P. Attané, and A. Marty. Soft-x-ray magnetic speckles from a nanostructured fepd wire. *Phys. Rev. B*, 66(17):172404, Nov 2002.

[6] Michael S. Pierce, Rob G. Moore, Larry B. Sorensen, Stephen D. Kevan, Olav Hellwig, Eric E. Fullerton, and Jeffrey B. Kortright. Quasistatic x-ray speckle metrology of microscopic magnetic return-point memory. *Phys. Rev. Lett.*, 90(17):175502, Apr 2003.

[7] W. H. Meiklejohn and C. P. Bean. New magnetic anisotropy. *Phys. Rev.*, 102(5):1413–1414, Jun 1956.

[8] K. Chesnel, E. E. Fullerton, M. J. Carey, J. B. Kortright, and S. D. Kevan. Magnetic memory in ferromagnetic thin films via exchange coupling. *Physical Review B (Condensed Matter and Materials Physics)*, 78(13):132409, 2008.

[9] T. L. Kirk, O. Hellwig, and Eric E. Fullerton. Coercivity mechanisms in positive exchange-biased co films and co/pt multilayers. *Phys. Rev. B*, 65(22):224426, Jun 2002.

[10] D. Mauri, H. C. Siegmann, P. S. Bagus, and E. Kay. Simple model for thin ferromagnetic films exchange coupled to an antiferromagnetic substrate. *Journal of Applied Physics*, 62(7):3047–3049, 1987.

[11] J. P. Hannon, G. T. Trammell, M. Blume, and Doon Gibbs. X-ray resonance exchange scattering. *Phys. Rev. Lett.*, 61(10):1245–1248, Sep 1988.

[12] S. Eisebitt, J. Luning, W. F. Schlotter, M. Lorgen, O. Hellwig, W. Eberhardt, and J. Stohr. Lensless imaging of magnetic nanostructures by x-ray spectroholography. *Nature*, 432(7019):885–888, Dec 2004.

[13] John Loomis. Cross correlation, June 2009. `http://www.engr.udayton.edu/faculty/jloomis/ece561/notes/xcorr/xcorr.html`.

[14] R. Gonzalez, R. Woods, and S. Eddins. *Digital Image Processing Using Matlab*. Prentice Hall, 2003.

[15] Frederic Patin. An introduction to digital image processing, June 2009. `http://www.gamedev.net/reference/programming/features/imageproc/page2.asp`.

[16] Robert Nowak. 2d dft, June 2009. `http://cnx.org/content/m10987/latest/`.

[17] F. Livet, F. Bley, R. Caudron, E. Geissler, D. Abernathy, C. Detlefs, G. Grübel, and M. Sutton. Kinetic evolution of unmixing in an alli alloy using x-ray intensity fluctuation spectroscopy. *Phys. Rev. E*, 63(3):036108, Feb 2001.

[18] S. Roy, M. R. Fitzsimmons, S. Park, M. Dorn, O. Petracic, Igor V. Roshchin, Zhi-Pan Li, X. Batlle, R. Morales, A. Misra, X. Zhang, K. Chesnel, J. B. Kortright, S. K. Sinha, and Ivan K. Schuller. Depth profile of uncompensated spins in an exchange bias system. *Phys. Rev. Lett.*, 95(4):047201, Jul 2005.

[19] M. S. Pierce, C. R. Buechler, L. B. Sorensen, J. J. Turner, S. D. Kevan, E. A. Jagla, J. M. Deutsch, T. Mai, O. Narayan, J. E. Davies, K. Liu, J. Hunter Dunn, K. M. Chesnel, J. B. Kortright, O. Hellwig, and E. E. Fullerton. Disorder-induced microscopic magnetic memory. *Phys. Rev. Lett.*, 94(1):017202, Jan 2005.